RESEARCH ARTICLE

Attenuation of the acoustic noise radiated by a compressible boundary layer through injection of a vibrationally active gas

Graeme I. Gillespie[1] · Stuart J. Laurence[1]

Abstract

The effects of vibrational nonequilibrium processes on turbulence-generated acoustic noise were investigated in a Mach-2.8 shock-tunnel facility. Gas mixtures with relevant absorption characteristics were first identified from measurements of attenuation coefficients using a heated acoustic chamber. In the shock-tunnel facility, CO_2, N_2, He, and He/CO_2 mixtures were injected into the lower boundary layer of the flow through a porous plate. A four-point Focused Laser Differential Interferometer (FLDI) positioned above the turbulent boundary layer was used to obtain simultaneous freestream measurements of entropic fluctuations propagating along streamlines and acoustic disturbances along Mach lines. Correlated fluctuations of Mach-line and streamline FLDI signal pairs were analyzed with a cross-power spectral density (CPSD). Compared to a boundary layer of pure air, the injection of 30%, 35%, and 40% He/CO_2 mixtures resulted in reduced fluctuation powers correlated along a Mach line in the frequency range of 200–800 kHz. Minimal reductions in fluctuation power were found along a streamline, indicating that the vibrationally active gas is affecting acoustic disturbances and not entropic disturbances. A mathematical disturbance model was created to examine the sensitivity of the measured attenuation to acoustic disturbances propagating from the lower boundary layer only. Disturbances were modeled as Gaussian wave packets of finite width, propagating in the streamwise direction and along Mach lines from the four walls of the test section. Modeling the acoustic disturbances from the lower boundary layer with a 15–30% amplitude reduction resulted in amplitude spectral densities and CPSDs that agreed well with the FLDI measurements.

1 Introduction

Turbulence-generated noise is of critical concern in the nozzle flows of conventional high-speed wind tunnels, where the noise environment encountered by models in the freestream is substantially stronger than that experienced in atmospheric flight and leads to much reduced transition Reynolds numbers. Laminar-turbulent transition has dramatic effects on heat transfer, skin friction, flow separation, and other aerodynamic properties (Pate and Schueler 1969; Schneider 2001). This complicates the use of conventional tunnels for studying hypersonic flow problems in which boundary-layer transition is important, and has led to the development of quiet tunnels, which provide low noise levels comparable to flight. These facilities incorporate special features to ensure that the nozzle boundary layer remains laminar, including

bleed slots upstream of the throat and long, polished nozzles (Schneider 2008). Although quiet flow facilities are well-suited for stability and transition research, conventional tunnels are still widely employed due to their accessibility, relatively inexpensive development, and range of operating Reynolds numbers. It is thus important to investigate control mechanisms that can reduce freestream noise levels in conventional high-speed facilities to allow for better comparison between experimental, computational, and flight test data.

Investigations into freestream disturbances in high-speed tunnels date back to Kovasznay (1953), who showed that small fluctuations in a viscous compressible flow can be described by three disturbance fields: entropy inhomogeneities, vortical perturbations, and acoustic waves. Morkovin (1957, 1959) expanded on the origin of the disturbance fields and discussed the relative importance of each, which can vary depending on the facility type. In reflected shock tunnels, entropy disturbances are known to originate in the reservoir and travel in the streamwise direction at the mean flow velocity, while acoustic disturbances are radiated from the turbulent boundary layers on the nozzle walls and propagate

✉ Graeme I. Gillespie
  ggilles@umd.edu

1 Department of Aerospace Engineering, University
  of Maryland, College Park, MD 20742, USA

into the freestream along characteristic Mach lines. Vorticity fluctuations originate upstream of the nozzle and result from the variation of the solenoidal component of the velocity field. In high-speed facilities, however, vortical fluctuation levels are often very low due to the large velocity ratio across the nozzle (Morkovin 1959), leaving entropic and acoustic disturbances as the primary contributions to freestream turbulence intensity. The current understanding of the origin of acoustic noise is based on the eddy Mach-wave concept of Phillips (1960), whereby radiation is produced from structures within the boundary layer moving supersonically with respect to the freestream. As the Mach number is increased, an increasing fraction of turbulent eddies acquire a relative supersonic velocity, leading to an increase in radiation intensity at higher Mach numbers. At Mach numbers of 2.5 or above, the acoustic disturbances are likely to dominate the disturbance environment (Laufer 1961, 1964). Therefore, mechanisms capable of attenuating acoustic radiation are of particular interest to high-speed facilities.

One possible mechanism for the attenuation of acoustic disturbances is molecular nonequilibrium processes. At temperatures above 3000 K, the internal energy modes of O_2 and N_2 molecules in air become excited, leading to molecular excitation–relaxation processes between internal (e.g., vibrational) and external (translational and rotational) degrees of freedom (Fujii and Hornung 2003). At lower temperatures, the vibrational and dissociational modes of air constituents freeze out; however, the vibrational modes of carbon dioxide and other polyatomic gases remain substantially excited even at room temperature. In the excitation–relaxation mechanism, the propagating acoustic wave excites vibrational energy states of the gas molecules, and the subsequent transfer of energy between internal and external modes occurs with a relaxation time that is dependent on the collisional dynamics, vibrational modes available, and gas constants, but is significantly longer than that required to achieve translational/rotational equilibrium. If the period of the acoustic wave is of the same order as the vibrational relaxation time, oscillations in the thermodynamic state of the gas remain out of the phase with the acoustic disturbance, resulting in significant attenuation and dispersion of the propagating waves (Clarke et al. 1964). To model such processes, theories on decoupling the multimode vibrational relaxation energy exchange in pure gases have been proposed by Bauer (1965), Bauer et al. (1972), Shields (1970), and Bass et al. (1972). More recently, Dain and Lueptow (2001) and Zhang et al. (2013) developed a vibrational relaxation model in ternary mixtures of polyatomic gases at room temperature, based on the coupled relaxation equations given by Schwartz et al. (1952) and Landau and Teller (1936). Despite this development in theoretical modeling of vibrational relaxation in certain gas mixtures, there remain limited experimental data for comparison and validation,

particularly at elevated temperature. The most recent comprehensive measurements of attenuation coefficients are from the work of Petculescu et al. (2006), which included mixtures of C_2H_4/N_2, CO_2/air, and CH_4/air at room temperature, and Ejakov et al. (2003), which featured O_2/N_2, CH_4/N_2, and CO_2/N_2 at room temperature.

Investigations of the effects of thermodynamic nonequilibrium on turbulence-related phenomena are rare. In the low-speed turbulent-channel-flow experiments of Fuller et al. (2014), N_2 was vibrationally excited using a radiofrequency plasma generation system; the plasma-induced nonequilibrium, thermal heating, and flow acceleration resulted in significantly reduced peak turbulence intensities and Reynolds shear stresses. Numerical simulations of canonical, subsonic turbulence-in-box (Neville et al. 2014), and triply periodic turbulent compressible shear layers (Neville et al. 2015) have also indicated that thermal nonequilibrium may have a significant effect on the fluid dilatation and temperature fluctuations in hot turbulent flows. In other studies, the effects of vibrational/dissociational relaxation on the transition process leading to turbulence have been examined. In particular, acoustic attenuation from nonequilibrium processes in CO_2 has been shown by Fujii and Hornung (2003), Leyva et al. (2009), and Jewell et al. (2013) to delay transition on a cone in the T5 hypervelocity shock tunnel at CalTech: this was attributed to damping of the second-mode disturbances which are primarily acoustic in nature and were assumed to be responsible for transition at these conditions. Similarly, a computational study by Elliott et al. (2019) found that the addition of CO_2 in freestream air was effective in reducing the amplification rates of disturbances in the boundary layer on a cone in high- and low-enthalpy flow in the same facility. While the studies just described highlight some aspects of the effects of nonequilibrium processes on transitional and turbulent flow phenomena, the effects of nonequilibrium on turbulence-generated acoustic radiation have not been reported to date. In the present context, acoustic disturbances in the frequency band 100 kHz–1 MHz are of particular interest, as this range is characteristic of the second-mode instability that often dominates transition on slender bodies at hypersonic conditions (Laurence et al. 2016).

From an experimental perspective, measurement of acoustic radiation in high-speed facilities is challenging. Pitot-pressure measurements suffer from limited bandwidth [Duan et al. (2019), for example, somewhat optimistically quotes an upper limit of 1 MHz] and the creation of bow shocks that modulate and filter flow features of interest (Mahesh and Lee 1995). Acoustic disturbance resonances within the stagnation region can also limit the useful bandwidth of Pitot measurements (Chaudhry and Candler 2017). Flush-mounted surface transducers meanwhile provide poor spatial resolution and are generally unsuitable for

measuring the noise level in a hypersonic freestream. Hot-wire anemometry (HWA) also exhibits a limited bandwidth. Kendall (1975), for example, quotes a maximum frequency of approximately 50 kHz in the freestream and 100–200 kHz within the boundary layer (limited by the frequency compensation circuit), while Demetriades (1989) and Stetson and Kimmel (1992) quote nominal bandwidths of 0–500 kHz and 0–600 kHz, respectively, for boundary layer measurements; however, the latter noted limited signal to noise at high frequencies and were unable to detect any boundary-layer disturbances above 300 kHz, suggesting a somewhat lower effective bandwidth. An additional concern in the current context is the inability of fragile fine-wire probes to withstand harsh testing environments such as those encountered in shock-driven facilities. Furthermore, both Pitot and HWA measurements are necessarily intrusive, limiting the ability to make simultaneous measurements at different locations within the flowfield.

An alternative diagnostic called Focused Laser Differential Interferometry (FLDI) provides a nonintrusive method for high-sensitivity, high-bandwidth measurements of tunnel noise (Parziale 2013). The technique was invented by Smeets and George in the 1970s (Smeets and George 1971, 1973, 1975; Smeets 1972, 1977) and is a nonimaging, polarizing interferometer that is sensitive to phase differences between two closely spaced probe volumes. The differences in phase are the result of varying densities at each FLDI probe; therefore, the measured voltage fluctuations are proportional to the density gradient between the two focal volumes. FLDI is capable of high-frequency response—generally to well above 1 MHz (Parziale et al. 2012)—with high spatial resolution (on the order of micrometers) and a high signal-to-noise ratio (SNR). The nonintrusive nature of this technique also allows multiple correlated points within the flowfield to be simultaneously interrogated. Additionally, the focusing ability of the FLDI allows unwanted signal to be rejected away from the flow features of interest at the instrument's focus. Detailed explanations of the working principle of FLDI can be found in Schmidt and Shepherd (2015), Parziale et al. (2014), Settles and Fulghum (2016), Fulghum (2014), and Ceruzzi and Cadou (2022).

In the present work, the effects of vibrational nonequilibrium on acoustic radiation from a turbulent boundary layer are investigated in Mach-2.8 flow. The overall methodology of the investigation is as follows. First, suitable gas mixtures that are vibrationally active at relevant conditions and over the frequency range of interest are identified from measurements of attenuation coefficients using a heated acoustic chamber (Gillespie and Laurence 2023). In a Mach-2.8 shock-tunnel facility, these gas mixtures (CO_2, CO_2/He, N_2, and He) are then injected into a turbulent boundary layer that has developed along the bottom wall of the test section. A four-point FLDI positioned above the turbulent boundary layer is used to obtain fluctuation measurements outside the boundary layer; by aligning probe pairs along both streamlines and Mach lines, the influence of entropic and acoustic disturbances can be (at least partially) separated, since only the latter are expected to be affected by the injection. A mathematical model is then constructed to aid in the interpretation of the measurements, in particular to isolate the contribution to the measured signal from the lower boundary layer.

2 Experimental methodology

2.1 Acoustic chamber design

Prior to injecting gas mixtures into a turbulent boundary layer, the attenuation properties of various mixtures must first be measured to identify mixtures capable of significant acoustic attenuation in the frequency range of interest (> 100 kHz) and at the relevant temperatures and pressures. A heated acoustic chamber was thus designed for attenuation coefficient measurements based on similar facilities from Winter and Hill (1967) and Wang and Springer (1973). As seen in Fig. 1, the heated chamber consists of two cylindrical Watlow ceramic fiber-radiative heaters surrounding a quartz tube. The 650-W cylindrical heaters had a 76.2 mm inner diameter, 177.8 mm outer diameter, and a total heated length of 304.8 mm. The heaters are wrapped in 25.4 mm thick, 128 kg/m^3 dense ceramic fiber insulation, and encased in a 12.7-mm-thick aluminum tube. Inside the 67-mm-diameter quartz tube, two quartz rods with a diameter of 22 mm and length of 635 mm are used as acoustic buffer rods to transmit and receive ultrasonic waves through the test gas. The ultrasonic waves were generated with a pair of Steminc piezoelectric transducers epoxied to the rod ends. The quartz rods are supported by optical posts on breadboards and are secured with shaft collars clamped around a protective neoprene rubber. The distance between the quartz rods was varied with a linear translation stage, controlled by a programmable servo motor (Thorlabs KDC101).

The linear translation stage allows for the attenuation coefficient of a gas to be found experimentally with the differential path method (Winter and Hill 1967; Wang and Springer 1973). The acoustic pressure, P_a, decreases with distance, z, from the emitter according to

$$P_a = P_{a,0} e^{-\alpha z}, \tag{1}$$

where $P_{a,0}$ is the amplitude of the acoustic wave at the emitter, and α is the attenuation coefficient (Ejakov et al. 2003). By varying the distance between the emitting and receiving transducers, the attenuation can be found from the slope of the natural logarithm of voltage amplitude [proportional to
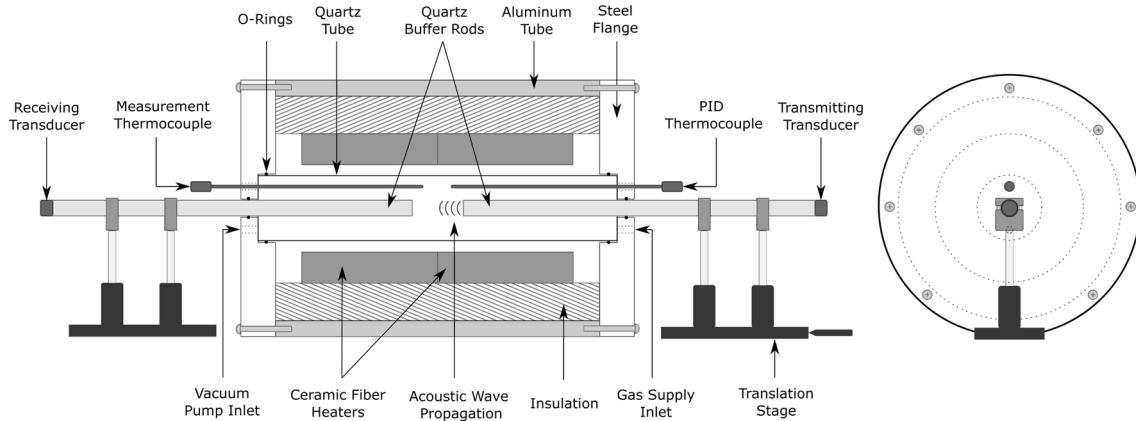
Fig. 1 Cross-section schematic of heated acoustic chamber for attenuation coefficient measurements (not to scale)

acoustic pressure (Ejakov et al. 2003)] as a function of separation distance.

A high-temperature thermocouple probe provides the control and high limit inputs into a PID controller. The thermocouple probe used is capable of measuring temperatures up to 1600 K with a response time of 0.55 s. The PID variables are tuned manually depending on the gas mixture and setpoint temperature. Using an NI DAQ module and LabVIEW program, a second high-temperature thermocouple probe provides continuous measurements of the chamber temperature. Pressure measurements are made with an Omega transducer located along the gas supply inlet tubing, sufficiently far from the high temperatures of the test gas.

Since the attenuation at a given temperature depends only on the ratio of frequency/pressure (Bhatia 1985), f/P, either the acoustic frequency or chamber pressure can be varied. It was determined that the transducers have the strongest voltage response at 50 kHz and 90 kHz; therefore, measurements were taken with these acoustic frequencies at chamber pressures varying from 1–0.75 atm at 50 kHz to 1–0.2 atm at 90 kHz. Transmitted signals consisted of 8 cycles at 90 kHz and 5 cycles at 50 kHz. At pressures lower than 0.2 atm, the signal-to-noise ratio (SNR) of the output voltage was too low for consistent measurements to be made. The rods are initially separated by approximately 20 mm, which was found to be sufficiently far as to not elicit a standing wave response, while still providing a high SNR. Further details of the acoustic chamber design are provided in Gillespie and Laurence (2023).

2.2 Shock-tunnel facility

Injection experiments were conducted in the HyperTERP facility at the University of Maryland (Butler and Laurence 2019). A schematic view of the facility is presented in Fig. 2. HyperTERP is a reflected-shock tunnel capable of operating at a variety of freestream enthalpy and unit Reynolds numbers through modification of the pressure and composition of the driver and driven gases. Although typically used with a Mach-6 free-jet nozzle, HyperTERP was operated with a newly developed Mach-2.8 nozzle and direct-connect test section, as detailed by Pee et al. (2021). Although a higher Mach-number flow would increase the fraction of relatively supersonic disturbances within the boundary layer and thus the acoustic radiation intensity, the requirements for the current experimental apparatus—in particular, a
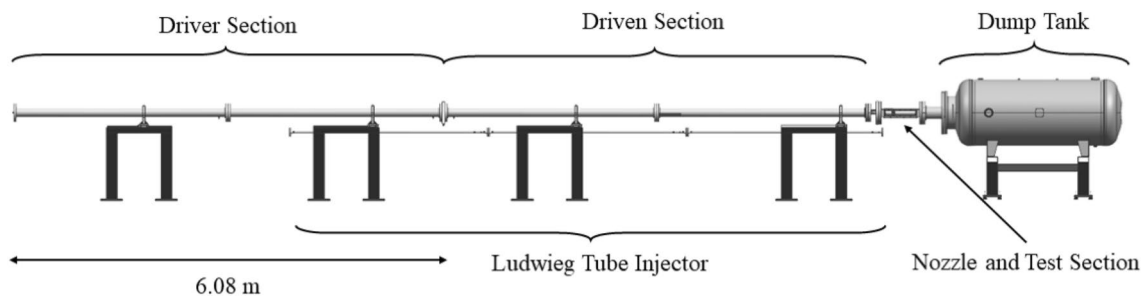

Fig. 2 Schematic of HyperTERP shock tunnel with direct-connect test section

two-dimensional, fully optically accessible test section with an extended run of a fully developed turbulent boundary layer—become increasingly difficult to satisfy as the Mach number is increased. A lower Mach number can also ensure that the boundary-layer temperatures are sufficiently high that the vibrational modes of CO_2 remain active.

The propagation speed of the incident shock wave is measured by four PCB 113B26 pressure transducers sampled at 100 kHz. The sensors are located at three different stations along the driven-tube wall, including two sensors located 8.9-cm upstream of the nozzle that serves as the reservoir measurement. The signals are conditioned using a PCB 482C05 signal conditioner. Following compression and heating by the incident and reflected shocks, the test gas (air) is accelerated through a planar contoured nozzle. The test section is shown in Fig. 3, which has a cross section of 50.8 mm × 50.8 mm and a total length along the tunnel axis of 606.5 mm. Optical access into the test section is provided by 12.7-mm-thick, NBK7-glass windows with dimensions of 88.9 mm × 50.8 mm and 285.8 mm × 50.8 mm in the upstream and downstream regions, respectively. Mean surface pressure measurements on the upper test-section wall were provided by a Kulite XCQ-062-1.7BARA transducer instrumented along the spanwise centerline at a distance of 57.2 mm from the leading edge of the upstream window. Through an analysis of the shock-tunnel reservoir and freestream pressures, it was determined that the Mach number of the nozzle was 2.82 ± 0.06, sufficiently high that frozen Mach radiation from the turbulent boundary layers should be the most significant contribution to the freestream noise (Laufer 1961).

Injection of the gas mixtures into the lower boundary layer of the flow was by means of a Ludwieg-tube-based injection system and porous plate. The Ludwieg tube consisted of a 8.31-m-long, 25.4-mm-diameter pipe connected to a ASCO 8210P093 fast-acting valve which controlled the flow into the injector assembly in the test section. Located in the upstream region of the test section, the injector assembly was a smooth channel that opened up to a small plenum underneath a porous plate; approximately 4 mm separated the porous plate from the top of the injector housing. The
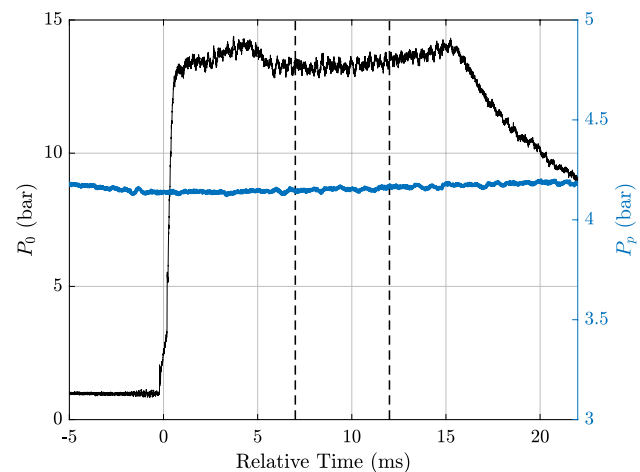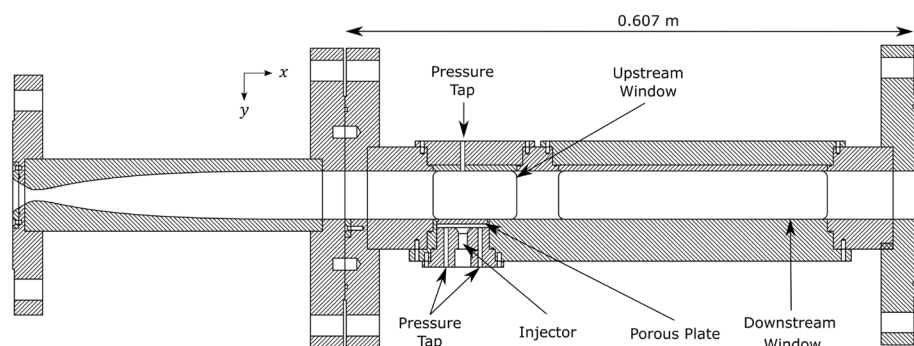
Fig. 4 Typical reservoir pressure trace (black) and injector plenum pressure (blue) for the case of CO_2 injection at 4.18 bar. The steady test time occurs between two dashed lines

porous plate consisted of a sintered stainless steel material with a PORAL grade of 5 (as defined by the manufacturer) and dimensions of 41.9 mm × 52.1 mm × 5 mm. The leading edge of the porous plate was a distance of 123 mm from the nozzle exit. At the location of the porous plate, the boundary layers along the walls were in a well-developed turbulent state.

During an experiment, the Ludwieg tube is held at a desired pressure until the fast-acting solenoid valve is opened. After opening, the pressure at the exit of the Ludwieg tube is nearly constant through the time taken for the initial expansion fan to traverse the length of the tube and back again; the tunnel operation is timed such that the steady test time occurs during the constant pressure period of the Ludwieg tube (Pee 2021). Two Kulite XCQ-093-250A pressure transducers were mounted upstream of the solenoid valve, with an additional two transducers installed in the injector plenum, underneath the porous plate; the signals were recorded at 100 kHz. A typical time trace of the reservoir pressure and injector plenum pressure is shown in Fig. 4 for CO_2 injection at 4.18 bar, where the steady test time occurs from 7 to 12 ms. For all injection conditions, the

Fig. 3 Schematic of the direct-connect test section with porous plate injector

plenum pressure had a standard deviation of less than 0.8% during the steady test time. The plenum pressure can be used to calculate the mass flow rate through the plate for a given gas mixture; this is discussed in "Appendix."

2.3 Shock-tunnel test conditions

The mean reservoir and freestream conditions are summarized in Table 1. For all parameters, the shot-to-shot standard deviation was greater than the standard deviation throughout the steady test time for a given shot. The reservoir and freestream pressure is measured directly, while all other parameters are calculated indirectly. To calculate these parameters, thermally perfect shock relations across the measured incident and reflected shocks provide the temperature jump caused by the incident shock. Assuming that the reflection of the incident shock results in a stationary contact surface, the initial reservoir conditions may be calculated. The gas in this theoretical state is then isentropically expanded or compressed (with a calorically imperfect gas model) to the instantaneous pressure recorded by the PCB sensors, yielding the instantaneous reservoir temperature (Butler 2021). Finally, the gas is expanded through the nozzle to the freestream conditions assuming a thermally perfect gas model with freezing at the nozzle throat. The standard deviations listed in Table 1 for T_∞, ρ_∞, U_∞, and Re_∞ are computed with error propagation from the Mach number uncertainty; the resulting standard deviations were considerably greater than those from shot-to-shot variation. During the steady test time (approximately 5 ms), the reservoir-pressure unsteadiness is typically 2%; shot-to-shot variation in the mean pressure is on the order of 1.3%, with systematic uncertainty (calibration and nonlinearity) estimated as 1.6%. The uncertainty in the reservoir temperature from the shock-speed measurement is 0.4% (Butler and Laurence 2021).

2.4 Shock-tunnel diagnostic techniques

A standard Z-type schlieren with a horizontal knife edge was employed to visualize the effect of injection on the external flowfield. The light source was a Cavilux HF laser with pulses of 20-ns duration. A Phantom v2640 was used to capture the

Table 1 HyperTERP test conditions

P_0 (bar)	13.6 ± 0.2
T_0 (K)	697 ± 4
P_∞ (bar)	0.51 ± 0.01
T_∞ (K)	272 ± 7
ρ_∞ (kg/m³)	0.62 ± 0.04
U_∞ (m/s)	932 ± 30
Re_∞ ($\times 10^6$ m⁻¹)	34 ± 2
M_∞	2.82 ± 0.06

images at a frame rate of 62 kHz and a resolution of 896×400 pixels. The qualitative results of the schlieren visualization are detailed in Sect. 4.1.

The primary diagnostic in this work was a four-point FLDI, used for the simultaneous measurement of entropic disturbances propagating in the streamwise direction and acoustic radiation propagating along Mach lines. Typically, acoustic radiation is interpreted as a wavefront propagating in the streamwise direction at the sound source velocity, with an inclination angle linked to the source velocity (Laufer 1961). This wavefront is the result of a superposition of acoustic waves that originate within the boundary layer at varying streamwise locations, and is a Mach wave in the frame of reference of the moving source. Note, however, that this interpretation relies on the assumption of a "frozen" disturbance source moving at constant velocity within the boundary layer. A more general description (relying only on the assumption of weak disturbances) treats the radiation at a given point in the flowfield as an arbitrary superposition of acoustic signals propagating along Mach lines of the freestream flow from a locus of upstream positions: hence the choice of the Mach line (rather than the velocity-dependent inclination angle) in the present work.

Compared to a single-point FLDI, the four-point system consists of two additional Wollaston prisms and polarizers, as well as three additional photodetectors. A schematic of the four-point FLDI is shown in Fig. 5, with the flow in the $+x$-direction: here, LS is the laser, C_1 is a plano-convex lens, H is a half-wave plate, P is a linear polarizer, W is a Wollaston prism, C_2 is an achromatic doublet lens, T are the test section windows, C_3 is a plano-convex lens, C_4 is a bi-convex lens, and D is a photodetector. A Cobolt Samba 532-nm laser was used at its maximum power output of 400 mW. C_1 had a focal length of 25 mm, C_2 was a 50.8-mm-diameter lens of focal length 80 mm, C_3 had a focal length of 25 mm, and C_4 had a focal length of 40 mm. The Wollaston prisms were custom made by United Crystals to produce splitting angles of 75 arcmin, 52 arcmin, and 8 arcmin for W_1, W_2, and W_3, respectively.

The orientation of the beam spacings on the focal plane of the four-point FLDI is seen in Fig. 6, where Δx_1 and Δx_2 represent the intra- and inter-pair spacing, respectively. The beam spacings were measured with a LBP2-HR-VIS2 beam profiler at the focal plane. To set the intra-pair spacing, Δx_1, the Wollaston prism W_3 is positioned a focal-length distance away from the field lens, C_2, such that

$$\Delta x_1 = 2f_{\text{FL},C_2} \tan\left(\frac{\epsilon_1}{2}\right), \tag{2}$$

where ϵ_1 is the splitting angle of prism W_1. From Eq. (2), $\Delta x_1 = 187\,\mu\text{m}$, and the FLDI was adjusted until this separation was attained ($\pm 8\,\mu\text{m}$). As seen in Fig. 6, Wollaston prism W_2 was used to split the beams along a Mach line,
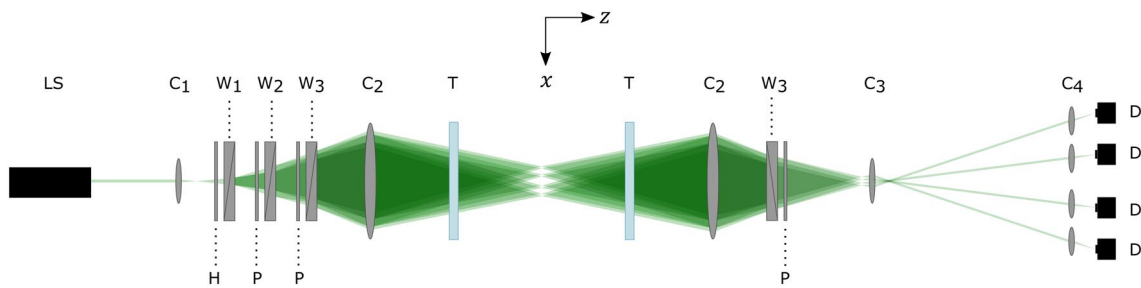
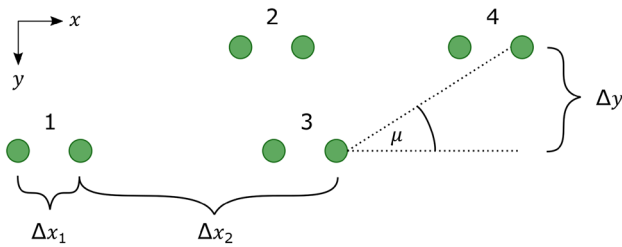**Fig. 5** Schematic of the four-point Focused Laser Differential Interferometer

Fig. 6 Beam spacing of the four-point Focused Laser Differential Interferometer, with $\Delta x_1 = 0.187 \pm 0.008$ mm, $\Delta x_2 = 1.070 \pm 0.008$ mm, $\Delta y = 0.365 \pm 0.008$ mm, and $\mu = 20.82 \pm 0.12°$

where μ is intended to be the Mach angle at Mach 2.82 (i.e., 20.77°). Using the beam profiler, the spacings were measured to be $\Delta x_2 = 1.070 \pm 0.008$ mm and $\Delta y = 0.365 \pm 0.008$ mm, giving $\mu = 20.82 \pm 0.12°$. The beam pairs were arranged such that the spacing between points 1–2 and 3–4 was approximately equal to Δx_2.

The FLDI beams propagate through the test section, where index of refraction gradients in the flow creates a phase shift between the beams. This results in a voltage fluctuation when passed through the final polarizer and into a photodetector. The FLDI signals were recorded by four DET36A2 biased Si photodetectors terminated with $50\,\Omega$ resistors. The signals were then digitized by a 14-bit Picoscope 5444D and sampled at 25 MHz. The relationship between the output voltage, measured phase change, and density gradient is outlined in Gillespie et al. (2022).

As a result of the beams being focused on the centerline of the test section, the relative size of the local beam radius and wavenumber leads to signal from the sidewall boundary layers being reduced. Low-wavenumber disturbances, however, may still be corrupted by sidewall boundary layers, while high wavenumbers are more representative of disturbances in the core flow region. Gillespie et al. (2022) present an analysis of this signal attenuation for a similar four-point FLDI in the Mach-6 configuration of the HyperTERP facility. An important parameter used when determining the influence of the sidewall boundary layers on the measured signal is the

Gaussian beam radius, ω. Defined as the radius at which the beam irradiance reaches $1/e^2$ of its peak, ω can be found at any point along the z-axis with

$$\omega^2(z) = \omega_0^2 \left[1 + \left(\frac{\lambda_0 z}{\pi \omega_0^2} \right)^2 \right], \tag{3}$$

where ω_0 is the radius at the focal point, and λ_0 is the wavelength of the light (Siegman 1986). In the far field, the beam divergence angle is given by

$$\theta = \frac{\lambda_0}{\pi \omega_0}. \tag{4}$$

In order to accurately measure the Gaussian beam radius at the focal plane of the system (ω_0), an estimate of the beam divergence angle must be computed from the slope of measured beam radii along the optical path, i.e., $\theta = \text{atan}(\Delta\omega / \Delta z)$. Since it is not possible to translate the beam profiler along the optical path inside the narrow test section, the FLDI was designed such that each half could be independently removed from the rail without altering any of the optical components. This allowed the beam radii to be measured on a benchtop, prior to installation around the test section. Using small optical windows to replicate the test section windows, the beam profiler was translated along the optical path with a manual translation stage. Images were taken at increments of 1 mm from $z - z_0 = [0 - 8]$ mm, where z_0 is the plane where the measured beam radius was the smallest. Beam intensity profiles of FLDI point 1 are seen in Fig. 7a at two locations. Gaussian curves were fit to each beam intensity profile, and the beam radius was found from $\omega = 2\sigma$, where σ is the standard deviation of the Gaussian distribution. From the slope of the beam radius as a function of $z - z_0$, the beam waist was calculated with Eq. (4) to be $\omega_0 = 2.5 \pm 0.5\,\mu$m. This differed slightly from the measured beam waist of 5.3 μm, which is likely due to the spatial limitation of the beam profiler resulting from its pixel size of $3.69\,\mu\text{m} \times 3.69\,\mu\text{m}$. Measurements of the beam radius along the z-axis are plotted in Fig. 7b with the fitted linear regression between $z - z_0 = [3 - 8]$ mm.

Fig. 7 a Beam intensity profiles at (left) $z - z_0 = 1$ mm and (right) $z - z_0 = 4$ mm, centered on FLDI point 1. **b** Measurements of the beam radius, ω, along the z-axis with a line of best fit ($R^2 = 0.9991$) to determine the radius at the focal point, ω_0

(a)

(b)
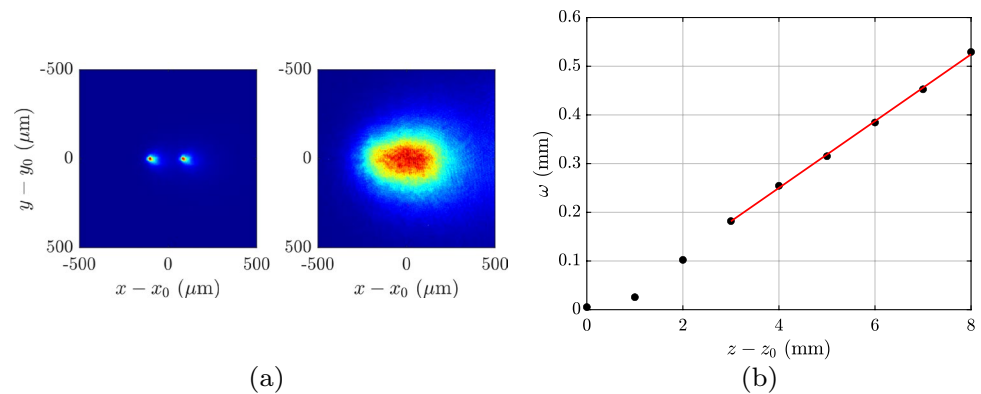
Prior to analyzing the FLDI measurements, the influence of the sidewall boundary layers on the FLDI signal must first be examined. To do so, the FLDI sensitivity transfer function developed by Ceruzzi and Cadou (2022) was applied to the four-point FLDI setup. Following the procedure detailed in Sect. 3.5 of Gillespie et al. (2022), a cutoff wavenumber is conservatively estimated, whereby disturbances with larger wavenumbers can be attributed to the core flow. In addition to properties of the FLDI (λ_0, ω_0, Δx_1), the calculation of the cutoff wavenumber is dependent on the sidewall boundary-layer thickness, half-width of the flow region (25.4 mm), and the ratio of frequency-averaged disturbance amplitudes of the sidewall boundary layers relative to the core flow. The sidewall boundary-layer thickness is assumed to be equal to that of the boundary layer along the top wall. As depicted by schlieren images of the flowfield in the vicinity of the FLDI focal points (detailed in Sect. 4.1), the boundary layer along the top wall has a thickness of approximately 10 mm.

To estimate the relative disturbance amplitudes in the sidewall boundary layer, previous studies by Zhang et al. (2018) and Lafferty and Norris (2007) are utilized. Zhang et al. (2018) found that the magnitudes of density-based turbulence intensity across all wavenumbers in a Direct Numerical Simulation (DNS) of a Mach-2.5 boundary layer were on the orders of 8–10%. In a summary of the AEDC 16-foot supersonic tunnel (PWT 16S) at Mach 2, 2.5, and 3, Lafferty and Norris (2007) found that freestream Pitot-probe RMS fluctuations were typically on the order of 0.7%, 1.5%, and 3%, respectively. In the AEDC VKF Tunnel A at Mach 3, Lafferty and Norris (2007) report a freestream RMS fluctuation of around 2–4%. Therefore, disturbances in the sidewall boundary layers are assumed to have a magnitude 3 times greater than those in the core flow. Substituting in the FLDI properties, sidewall boundary-layer thickness, half-width of the flow region, and disturbance amplitude ratio into the procedure outlined by Gillespie et al. (2022), a cutoff wavenumber of $k \approx 3200$ m^{-1} is conservatively estimated. Therefore, disturbances with $k > 3200$ m^{-1} can be attributed to the

core flow without any signal corruption from the sidewall boundary layers.

3 Acoustic chamber results

Mixtures of CO_2/He are of particular interest for the shock-tunnel experiments, since the addition of He in CO_2 has been previously shown by Lewis and Shields (1967) to increase the frequency of peak attenuation in CO_2. This is likely caused by the light He molecules acting as an efficient collision partner with CO_2, resulting in lower relaxation times for the mixture (Lewis and Shields 1967). Therefore, mixtures of CO_2/He could potentially be used to adjust the attenuation to certain desired frequency ranges. For this reason, the acoustic chamber experiments focused on these mixtures. The attenuation coefficients of CO_2 and CO_2/He mixtures at elevated temperatures were measured with an acoustic chamber. As discussed in Sect. 2.1, the attenuation coefficient is found by varying the distance between the piezoelectric transducers and measuring the voltage output from the receiving transducer. The power of the output signal at the acoustic frequency, P_f, is computed with a power spectral density (PSD). The corresponding amplitude is then plotted as a function of separation distance between the rods, and the attenuation is found from the slope of the natural logarithm of the amplitude. In Fig. 8, the natural logarithm of the output signal amplitude, normalized by the amplitude at the initial separation distance z_0, is plotted as a function of normalized distance between the rods for CO_2 at 293 K and various pressures. In each case, a line of best fit is plotted in red. For the 90-kHz signal shown here, decreasing the pressure below 1 atm results in a decrease in the attenuation coefficient. For each mixture and pressure, the temperature throughout the tests had a standard deviation less than 4 K. As a result of the temperature variations and slight change in chamber volume throughout the tests, the pressure varied by approximately ± 0.5%. For all attenuation coefficients presented in this section, an uncertainty of ± 7%
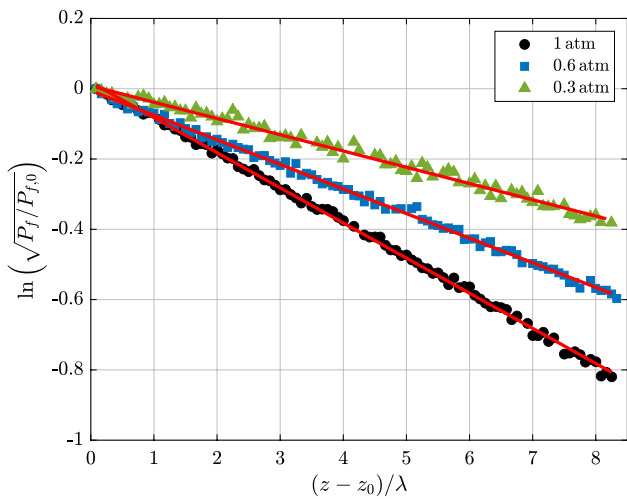
Fig. 8 Natural logarithm of the normalized output signal amplitude at 90 kHz as a function of distance between the rods, normalized by wavelength, for CO_2 at 293 K and various pressures. For each case, a line of best fit is shown in red

is conservatively estimated from the standard deviation of repeated measurements in the acoustic chamber.

The attenuation per wavelength, $\alpha\lambda$, for mixtures of CO_2 with 10%, 20%, and 40% He at 293 K is shown in Fig. 9a with a theoretical attenuation model for pure CO_2. Developed by Dain and Lueptow (2001) and Zhang et al. (2013), the attenuation model includes vibrational relaxation theory, classical attenuation, and diffusional attenuation. The model is seen to underpredict the measured attenuation coefficients but match the peak attenuation frequencies well; this underprediction was also noted by Ejakov et al. (2003), who stated that the discrepancy could be the result of the linear structure of the CO_2 molecule not being adequately accounted for

in the collisional dynamics model. Increasing the percentage of He in CO_2 resulted in an increase in the peak attenuation frequency and a slight decrease in the peak attenuation. The increase in peak attenuation frequency is likely caused by the light He molecules acting as an efficient collision partner with CO_2 (Lewis and Shields 1967), while the decrease in peak absorption can be attributed to the decrease of CO_2 in the mixture. Although there is limited literature to compare to, the peak attenuation of 10% He/CO_2 ($\alpha\lambda = 0.133$ at $f/P = 100$ kHz/atm) agrees well with the work of Lewis and Shields (1967), who reported a peak attenuation of $\alpha\lambda = 0.13$ at $f/P = 100$ kHz/atm for a mixture of 11% He/CO_2 at 298 K.

The attenuation spectra for pure CO_2 and mixtures of CO_2 with 20% and 40% He at 293–529 K are presented in Fig. 9b. For pure CO_2, a significant increase in attenuation is seen as the temperature is changed from 293 K to 373 K. As the temperature is increased further, the rate of increase of the peak attenuation drops until asymptoting at $\alpha\lambda \approx 0.255$ at 528 K. The peak attenuation frequency also increases to $f/P = 90$ kHz/atm. Other high-temperature attenuation results of CO_2 are limited to the work of Shields (1959) and Bass (1973) who found peak attenuation values of $\alpha\lambda = 0.22$ at $f/P = 90$ kHz/atm and 578 K, and $\alpha\lambda = 0.21$ at $f/P = 100$ kHz/atm and 600 K, respectively. Similar trends are seen for mixtures of 20% He in CO_2 at high temperatures, though the increase in peak absorption is not as significant. As the temperature is increased to 529 K, the peak attenuation reaches a value of $\alpha\lambda = 0.20$ at $f/P = 300$ kHz/atm. For mixtures of 40% He in CO_2, the attenuation appears to asymptote at lower temperatures, with a negligible change upon increasing the temperature from 423 K to 479 K. In the shock-tunnel experiments, the boundary-layer temperatures are expected to range from 272 K in the freestream to 293 K
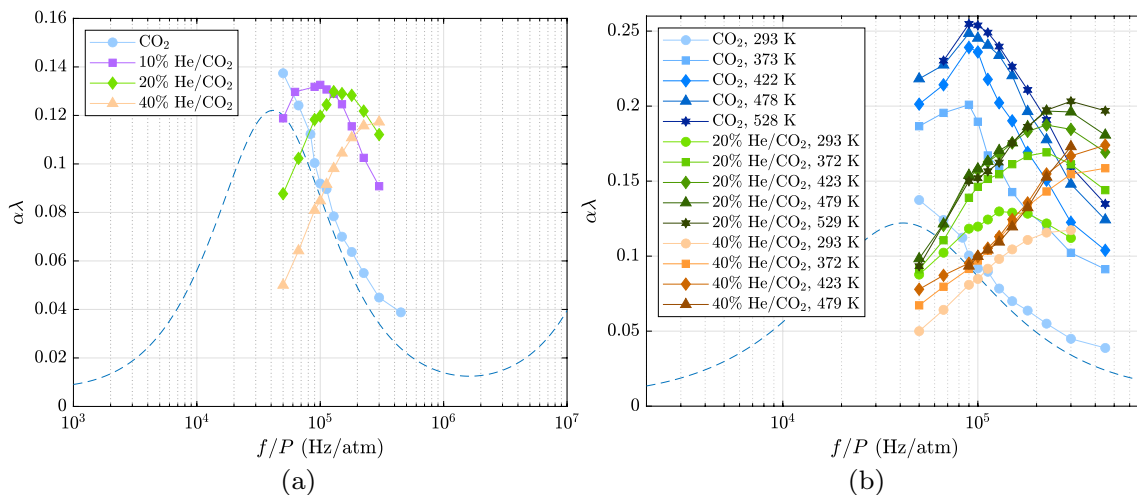

Fig. 9 Attenuation spectra of CO_2 and mixtures of CO_2 with **a** 10%, 20%, and 40% He at 293 K and **b** 20% and 40% He at 293–529 K. The theoretical attenuation model for CO_2 at 293 K is plotted as a dashed line (Dain and Lueptow 2001; Zhang et al. 2013)

at the wall (due to the short test time) with a maximum of approximately 372 K inside the boundary layer. This temperature profile is discussed further in "Appendix."

4 Shock-tunnel results

4.1 Injection conditions

The shock-tunnel test campaign consisted of multiple shots at various injection conditions, summarized in Table 2, where P_p is the mean pressure in the injector plenum during the steady test time and the gas mixtures are expressed as percentages by volume. As discussed in Sect. 3, mixtures of CO_2/He could be used to shift the attenuation to certain desired frequency ranges by varying the helium percentage; therefore, the injection conditions primarily consist of

Table 2 Injection conditions

Injection gas	P_p (bar, $\pm 0.8\%$)	Number of shots
None	N/A	12
50% He/CO_2	4.82	2
45% He/CO_2	3.98	3
40% He/CO_2	4.73	4
40% He/CO_2	3.99	3
40% He/CO_2	3.60	3
35% He/CO_2	4.14	3
35% He/CO_2	3.89	3
30% He/CO_2	3.87	3
30% He/CO_2	3.48	3
25% He/CO_2	4.14	3
25% He/CO_2	3.86	3
CO_2	4.18	3
CO_2	3.89	6
He	4.04	3
N_2	4.23	3
N_2	3.95	3

various CO_2/He mixtures. Additionally, injection of N_2 is used to ensure that the injection process itself is not responsible for any measured effects, and the injection of pure He is used to examine the effects of mean sound-speed gradients in the boundary layer that would also be present (to a lesser degree) in CO_2/He mixtures.

The schlieren system described in Sect. 2.4 was first used for visualization through the upstream window under quiescent conditions to ensure that the injection process through the porous plate was uniform and no leaks occurred around the plate's perimeter. The injection was then imaged in flow-on experiments for various gas mixtures and plenum pressures to determine the maximum pressure that could be injected such that the external flowfield was not significantly affected. Examples of flowfield are seen in Fig. 10 for the cases of no injection, injection of He at 4.04 bar, and injection of He at 7.28 bar. It should be noted that there is a crack in the top left corner of the window, obstructing a small region of the flowfield. With no injection, weak shocks are generated by small discontinuities on the upstream and downstream sides of the porous plate insert. The weak shock at the leading edge of the plate is slightly steepened by approximately 2° (relative to the no injection case) for He injection at 4.04 bar, while it is significantly affected at 7.28 bar injection. If the weak shock generated at the leading edge of the porous plate is steepened by greater than 15% (approximately 3°), then the plenum pressure is deemed to be too high. Therefore, 4.04 bar was chosen as the maximum plenum pressure for He injection. While this is an arbitrary criterion, it was found to be an appropriate measure of the effect of injection on the external flowfield. This criterion was used for all injection conditions.

The flowfield in the downstream window was imaged for a variety of injection gases and pressures in order to locate an area above the lower boundary layer in which to position the FLDI focal points. As a result of the narrow flowpath, weak shocks generated by small discontinuities along the test section are reflected downstream. The focal points of the FLDI should be positioned in a region that does not contain these shocks, since fluctuating weak shocks would
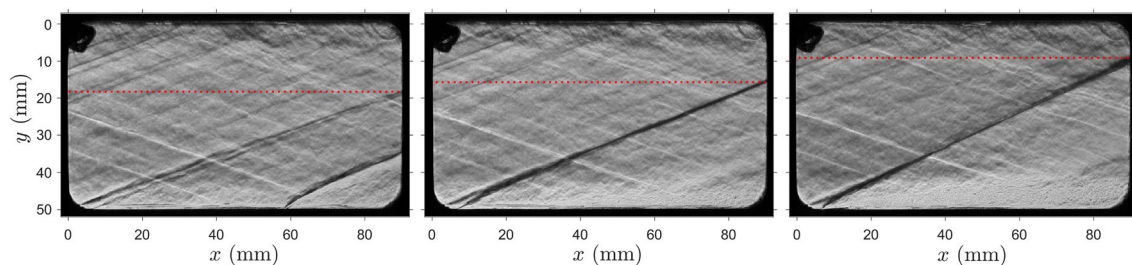

Fig. 10 No injection (left), injection of He at 4.04 bar (middle), and injection of He at 7.28 bar (right). To illustrate the steepening of the weak shock, a dotted red line indicates the y-position at which the shock meets the trailing edge of the upstream window

overwhelm the signal from freestream disturbances. A consistent area of clean flow for all injection conditions was identified 93.5 mm from the trailing edge of the downstream window, and 19.4 mm above the bottom wall, as shown in Fig. 11 for CO_2 injection at 3.89 bar.

4.2 FLDI convection velocity

Using the procedure described by Gillespie et al. (2022), the streamwise convection velocities were analyzed with a cross-correlation of the streamwise FLDI signal pairs 1–3 and 2–4, computed over consecutive 1-ms intervals throughout the 5-ms test time. For each injection condition, no significant differences in mean convection velocity were found, which is consistent with a negligible effect of injection on the external flowfield. Across all shots, the measured convection velocity is $\langle U_c \rangle = 627 \pm 31$ m/s, where the standard deviation is computed from the square root of the
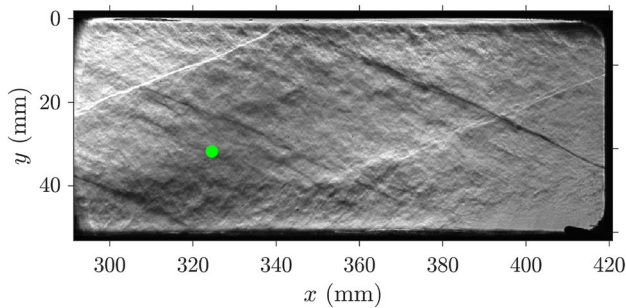
mean variances from each shot. This is below the theoretical freestream velocity of 932 m/s, with an average percent difference of -33%. The measured FLDI convection velocities are expected to be lower than the theoretical freestream velocity, since the FLDI is unable to reject all of the low wavenumber eddies convecting in the shear layer along the optical path, and inclined frozen Mach radiation originating upstream in the turbulent boundary layers will not be convecting at the local flow velocity. Note, for example, that Laufer (1961) conducted freestream HWA studies at Mach 1.6–5 and found that acoustic radiation from turbulent boundary layers had a source velocity ranging between 40 and 50% of the freestream velocity. The convection velocities measured here are similar to those by Ceruzzi (2022), who used two-point FLDI to measure freestream convection velocities in a Mach-18 flow and found mean propagation speeds ranging between 52 and 84% of the freestream.

4.3 FLDI fluctuations

For each condition listed in Table 2, the FLDI voltage signals were converted to phase fluctuations as described in Gillespie et al. (2022). The power spectral density (PSD) of the phase fluctuations was then calculated using Welch's method with Hanning windows of length 278 µs and 50% overlap, and the amplitude spectral density (ASD) was computed from the square root of the PSD. In Fig. 12a, we present the four ASDs, together with the measurement noise floor, for a shot without injection. We see that the ASDs are essentially identical for each of the four FLDI points; similar consistency was found for all shots. A straight line with slope -1.75 (which would correspond to -3.5 for the PSD) is also plotted for reference, which is a freestream spectra roll-off that has been reported in pressure data by numerous

Fig. 11 The location of the FLDI focal point in relation to a schlieren image of flow features in the downstream window from the injection of CO_2 at 3.89 bar. The x-axis is relative to the leading edge of the upstream window
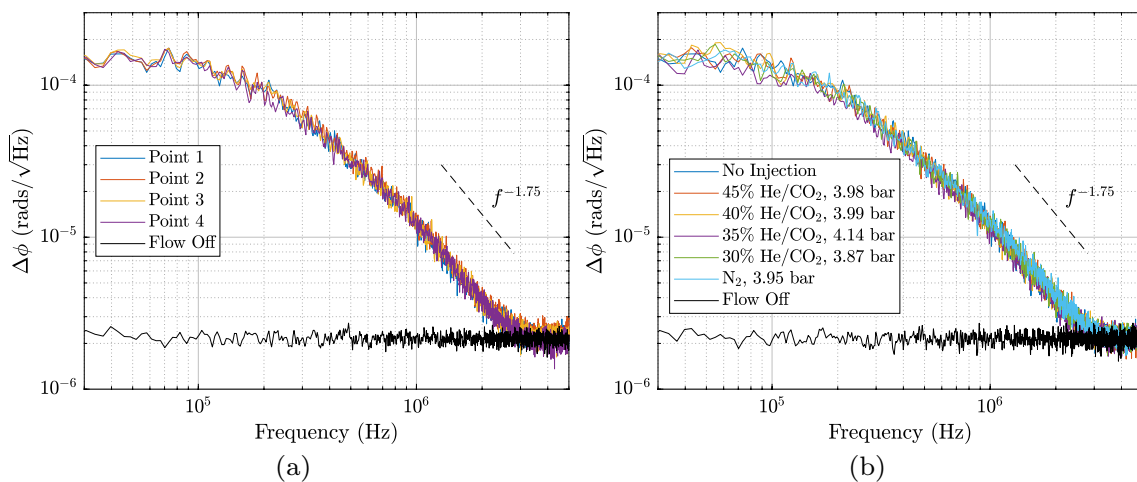

Fig. 12 Amplitude spectral density of phase fluctuations from **a** FLDI points 1–4 without injection and **b** FLDI point 1 for various injection conditions

authors, as summarized by Duan et al. (2019); we see that it also provides a reasonable match to the high-frequency data here. In Fig. 12b we show the ASDs of the phase fluctuations from FLDI point 1 for various injection conditions. When compared to the case without injection, no obvious attenuation in the disturbance fluctuations is seen for the injection shots. Although this might lead one to conclude that there is no attenuation present, we note that the ASDs at a single FLDI point incorporate noise contributions propagating from the bottom, top, and sidewall boundary layers, as well as entropic disturbances propagating in the streamwise direction. Therefore, the acoustic fluctuations propagating from the bottom boundary layer must be isolated to analyze the relevant acoustic attenuation. Importantly, however, the injection experiments (including the reference N_2 case) do not result in an increase in fluctuation amplitude, indicating that the injection process itself is not significantly affecting the freestream disturbance levels.

In order to isolate the contributions to the overall noise from the lower-wall boundary layer and freestream entropic disturbances, the cross-power spectral density (CPSD) was computed for the Mach-line and streamline signal pairs. The CPSD for a representative signal pair a-b is defined as

$$S_{ab}(f) = \sum_{m=-\infty}^{\infty} R_{ab}(m)e^{-j2\pi fm}, \tag{5}$$

where S_{ab} is the distribution of power per unit frequency for the correlated signal pair. The CPSD was calculated for Mach-line and streamline signal pairs using Welch's method with Hanning windows of length 33 µs and 50% overlap. For the calculation to be physically representative, we must account for the different times taken for the relevant disturbances to propagate between probe pairs (owing to both differing distances and propagation speeds). For streamline pair 1–3 or 2–4, this delay was specified as $\Delta t_{13,24} = \Delta x_2/U_\infty$, while for Mach-line pair 1–2 or 3–4, the delay was

$$\Delta t_{12,34} = \frac{\Delta y/\sin\mu}{\sqrt{U_\infty^2 - a_\infty^2}}, \tag{6}$$

where $\Delta y = 0.365$ mm (Fig. 6) and a_∞ is the theoretical freestream sound speed. Upon calculating the CPSD for each Mach-line pair and injection condition, Welch's t test was used to determine whether there was a significant difference between the CPSD with and without injection at any particular frequency. Welch's t test assumes the data sets have normal distributions, unequal variances, and unequal sample sizes, which are valid assumptions for the CPSD measurements.

Ideally, the correlated signals from FLDI pair 1–2 or 3–4 would consist uniquely of acoustic disturbances and that of pair 1–3 or 2–4 of entropic disturbances; however, in reality, these signals will not be completely independent due to the close proximity of the measurement points. Nevertheless, if we make the reasonable assumption that the relative dependence is consistent across all shots, the relation between the correlated fluctuations obtained from a Mach-line and streamline signal pair will illustrate the relative contributions of acoustic and entropic noise when compared to other shots.

Relative to shots without injection, the injection conditions that resulted in the most significant attenuation from the correlated Mach-line signals were 30% He/CO_2 at 3.87 bar, 35% He/CO_2 at 4.14 bar, and 40% He/CO_2 at 3.99 bar. The mean CPSDs of these mixtures compared to the no-injection case are seen in Fig. 13 for the Mach-line pair (Fig. 13a, c, e) and streamline pair (Fig. 13b, d, f), respectively. For all shots, there were minimal differences between the Mach-line signal pairs 1–2 and 3–4, and streamline signal pairs 1–3 and 2–4; therefore, the signal pairs 1–2 and 1–3 were typically used for analysis.

In Fig. 13, the mean CPSDs are plotted with the standard deviation from all shots at that condition. Markers indicate the frequencies at which the means are unequal with 95% confidence intervals, as determined by Welch's t test, and for which we therefore conclude that there is statistically significant difference between injection and no-injection cases. For a given injection condition, it can be seen that the correlated signals along the Mach line have higher fluctuation powers than those along a streamline. Thus, the acoustic disturbances have a higher coherence than entropic disturbances and, considering there are contributions from all four walls, will dominate the noise environment (Gillespie et al. 2022). For 30% He/CO_2 in Fig. 13a, a clear reduction in the Mach-line CPSD is measured relative to the case without injection, particularly at frequencies above 300 kHz. In Fig. 13b, however, no significant reductions are measured for fluctuations correlated along the corresponding streamline. This indicates that the vibrationally active gas species in the boundary layer is affecting acoustic radiation but not entropic disturbances, as expected. Similar results are found for 35% He/CO_2 (Fig. 13b, c) and 40% He/CO_2 (Fig. 13e, f), where a statistically significant attenuation is measured for the Mach-line fluctuations, with lesser or zero attenuation for the streamline fluctuations. Injection of 45% and 50% He/CO_2 resulted in a mean Mach-line CPSD with smaller fluctuation powers than the no-injection case; however, these differences were not statistically significant. A similar result occurred with the injection of 25% He/CO_2, but the difference was smaller still.

Turning to the reference injection cases, the mean CPSDs for injections of pure CO_2, He, and N_2 are presented in Fig. 14. Markers indicate the frequencies at which the mean CPSD from a given injection condition is statistically unequal to the mean CPSD without injection, where blue

Fig. 13 Mean cross-power spectral densities of phase fluctuations along a Mach line (**a**, **c**, **e**) and streamline (**b**, **d**, **f**) for injection of 30%, 35%, and 40% He/CO_2 mixtures compared to the case of no injection. Markers indicate the frequencies at which the means are unequal with 95% confidence intervals

(a)

(b)

(c)

(d)

(e)

(f)
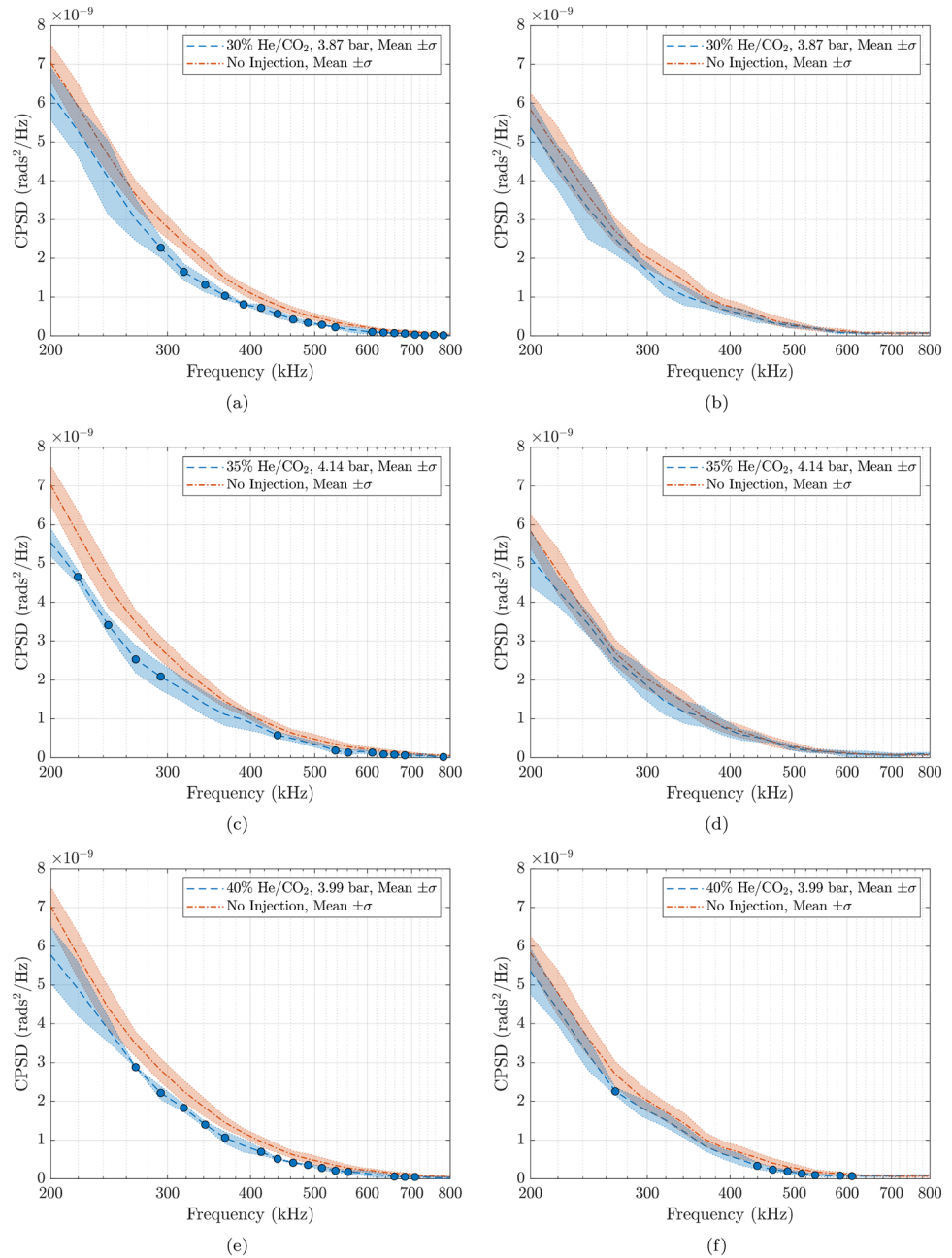
and red markers represent a decrease and increase in correlated fluctuation power, respectively. For the case of CO_2 and N_2, circular and square markers represent the higher and lower injection pressures, respectively. In Fig. 14a, no attenuation in acoustic fluctuations is measured for the injection of pure CO_2. Similarly, no attenuation in streamwise disturbances is measured in Fig. 14b, with instead a slight increase in fluctuation power occurring for CO_2 injection at 4.18 bar. A discussion as to why attenuation is observed along a Mach line for He/CO_2 mixtures but not pure CO_2 is presented in Sect. 4.4. For He injection in Fig. 14c, d, a small reduction in acoustic fluctuation powers is measured

at high frequencies, while no reductions are measured for the entropic disturbances. Although we would not expect any vibrational nonequilibrium processes to occur for a monatomic gas, it is possible that the large density gradient in the boundary layer created by the light He molecules could lead to trapping of acoustic waves; however, it is unclear whether this mechanism is responsible for the small attenuation measured. Such effects would be less pronounced in the mixtures, since the fraction of He is lower. For N_2 injection in Fig. 14e, f, essentially no attenuation was measured in the Mach-line CPSDs, with a slight increase in fluctuation powers for streamline correlations at the higher injection

Fig. 14 Mean cross-power spectral densities of phase fluctuations along a Mach line (**a**, **c**, **e**) and streamline (**b**, **d**, **f**) for injection of CO_2, He, and N_2 compared to the case of no injection. Markers indicate the frequencies at which the means are unequal with 95% confidence intervals
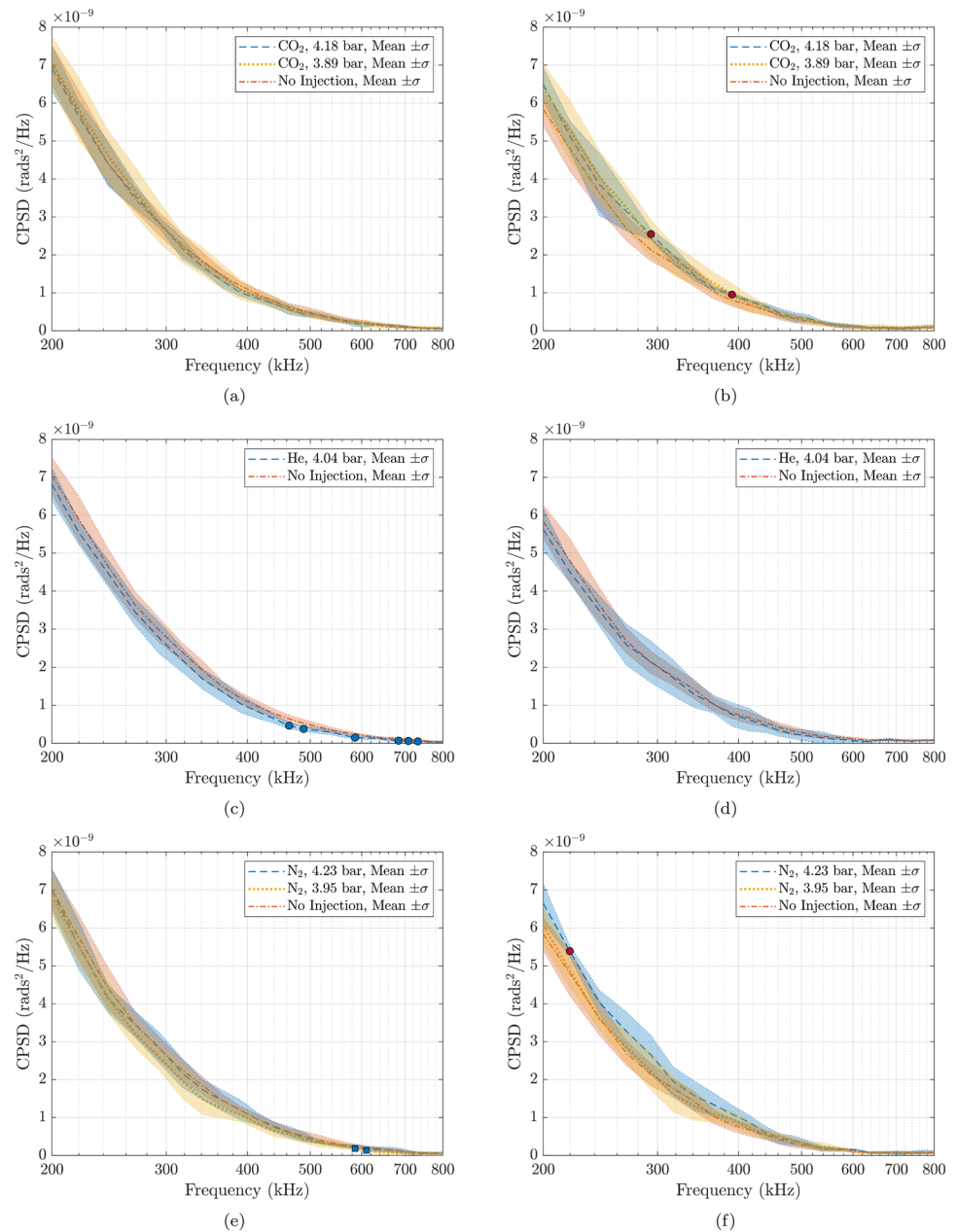
pressure. The lack of acoustic attenuation for the injection of N_2 further indicates that the injection process itself is not responsible for the attenuation measured in He/CO_2 mixtures (Fig. 13).

4.4 Comparison between attenuation spectra and FLDI measurements

Since attenuation of acoustic fluctuations was measured for 30%, 35%, and 40% He/CO_2 mixtures, but no reductions were observed in pure CO_2, this may be explained by the shifted attenuation spectra of He/CO_2 mixtures. To better understand the effect of increasing He fraction in CO_2,

the attenuation spectra obtained from the acoustic chamber (Fig. 9a) are re-examined here. In Fig. 15a we show the attenuation spectra of CO_2 and He/CO_2 mixtures at 293 K, with the theoretical attenuation model of CO_2 (Dain and Lueptow 2001; Zhang et al. 2013) scaled and shifted in each case to match the experimental measurements. This scaled theoretical model allows for the attenuation coefficient measurements to be extrapolated to a wider range of *f/P* values. The scaled model can then be used to estimate the attenuation from acoustic wave propagation through a gas mixture of a given thickness and pressure and, in particular, a simulated boundary layer with injected gas
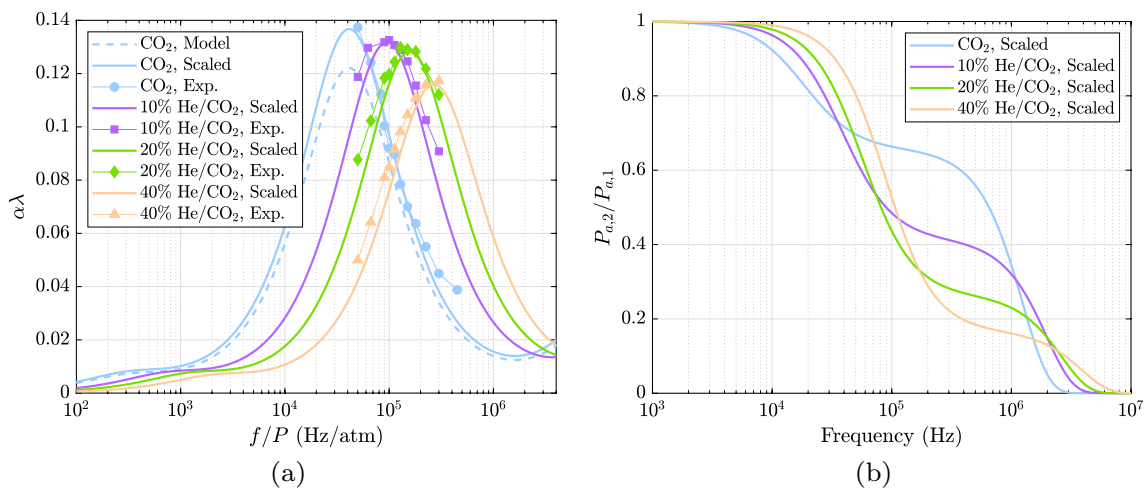
Fig. 15 **a** Attenuation spectra of CO_2 and mixtures of CO_2 with 10%, 20%, and 40% He at 293 K with theoretical attenuation of CO_2 scaled to match experimental results. **b** Theoretical acoustic pressure ratio across a 10-mm-thick gas layer at 0.51 bar

present. From Eq. (1), the ratio of acoustic pressures across a gas mixture of height δ is given by

$$\frac{P_{a,2}}{P_{a,1}} = e^{-\alpha\delta}. \qquad (7)$$

The approximate boundary-layer height was determined from schlieren images of the flowfield in the vicinity of the FLDI focal points, which depicts $\delta \approx 10$ mm. The attenuation spectra can then be plotted as the ratio of acoustic pressures as a function of frequency by substituting in δ and the freestream pressure. Seen in Fig. 15b, an increase in He fraction results in a large increase in attenuation in the frequency range of 200–800 kHz. This frequency range is also where significant attenuation was measured from fluctuations correlated along a Mach line in 30%, 35%, and 40% He/CO_2 mixtures (Fig. 13a, c, e), while no attenuation was measured for pure CO_2 (Fig. 14a). Since the temperature in the boundary layer is expected to range from approximately 272–372 K (as detailed in "Appendix"), the theoretical attenuation model was also scaled and shifted to match attenuation spectra obtained at 373 K (Fig. 13a). These results are not shown, but similar to the attenuation spectra at 293 K, an increase in helium fraction at 373 K results in a considerable increase in attenuation in the frequency range of 200–800 kHz. Therefore, the trends in measured attenuation coefficients at the expected boundary-layer temperatures are consistent with the findings of the shock-tunnel experiments.

In comparing Fig. 13a, c, e to a, however, it should be kept in mind that the measured attenuation from a correlated Mach-line signal may also be affected by the FLDI instrument itself. As discussed in Sect. 2.4, the low-frequency components of the FLDI signal may be corrupted by sidewall boundary layers, whereas high-frequency fluctuations

are more representative of disturbances in the core flow. Therefore, by shifting the attenuation spectra to higher frequencies, the FLDI is more sensitive to freestream acoustic disturbances affected by the vibrationally active gas species. To examine this, we must revisit the discussion of cutoff wavenumber, which was conservatively estimated as $k_x \approx 3200$ m^{-1}. Using the measured convection velocity of $\langle U_c \rangle = 627$ m/s, the frequency associated with this cutoff wavenumber is $f_c = \frac{k \langle U_c \rangle}{2\pi} \approx 319$ kHz. Disturbances above this frequency can be attributed to the core flow and are not corrupted by disturbances in the sidewall boundary layers. In Fig. 13, the measured reductions in correlated fluctuation amplitudes along the Mach line typically occurred at frequencies of 300 kHz and higher, which is consistent with this estimated cutoff frequency.

In Fig. 15b, we note a predicted reduction in acoustic pressure fluctuations of up to approximately 80%, which is significantly larger than was seen in Fig. 13. Note, however, that this analysis has assumed that the boundary layer consists exclusively of CO_2/He mixture, whereas the mass flux estimates provided in Appendix A suggest the fraction of CO_2/He to be significantly less than 50%. We additionally note that Fig. 15b assumes all acoustic waves are propagating through the vibrationally active gas species, whereas, because of the relatively close probe spacing, the correlated measurements along a Mach line are not completely independent of acoustic disturbances propagating from the top and sidewall boundary layers, and entropic disturbances propagating in the streamwise direction. Thus, the attenuation measured from correlated Mach-line signals is not as substantial as what is predicted by the theoretical attenuation spectra and it is difficult to quantify precisely the degree of attenuation within the lower boundary layer. This motivates the development of a mathematical disturbance model to

provide greater insight into the sensitivity of the measured attenuation to disturbances from the lower boundary lower only.

5 Disturbance model

A theoretical model was developed to replicate the dynamics of the disturbance environment in the freestream flow, incorporating both entropic and acoustic disturbances propagating through the FLDI focal points. The methodology employed is as follows. First, a model is constructed incorporating the primary disturbance types expected to be present in the shock-tunnel experiments, but with several free parameters. Second, the model parameters are tuned to match the experimental FLDI results for the case of no injection. Finally, the amplitudes of the acoustic disturbances from the lower boundary layer in the model are then reduced until the corresponding CPSD curves match those from the FLDI results for the injection of 30%, 35%, and 40% He/CO_2. Although the disturbance generation process is not directly modeled, the resulting disturbance field is consistent with the known physics of the problem, and we expect the comparison of reference and reduced disturbance fields to be physically meaningful.

The coordinate system of the model is shown in Fig. 16, where the propagation direction is described by angles ζ and η oriented in perpendicular planes. The disturbances are modeled as Gaussian wave packets propagating in five different directions: entropic disturbances propagating in the streamwise direction and acoustic disturbances propagating along Mach lines from the four walls of the test section. For each entropic and acoustic disturbance, a Gaussian width is prescribed in the direction perpendicular to its propagation, within the same plane as the wave packet. Therefore, for a wavevector propagating in the xy-plane ($\eta = 0$), the amplitude and phase will be constant along the z-axis at a given instant in time. While the disturbances are modeled in three-dimensional space, the simulated FLDI signals are obtained at the focal points only, i.e., the FLDI is not modeled as an integrated signal along the optical axis (z). This is acceptable for our purposes since the model will be tuned to match the experimental signals, and we are not attempting to recreate the measurement environment in its entirety. The composite freestream-disturbance signal is therefore recorded at locations corresponding to FLDI points 1, 2, and 3 (Fig. 6) along the centerline of the test section; FLDI point 4 is redundant.

The wave packets are created by multiplying three components together: planar waves, a pulse train of Gaussian curves, and a Gaussian curve oriented perpendicular to the propagation axis. A generalized time-varying plane wave propagating in three-dimensional space can be modeled by
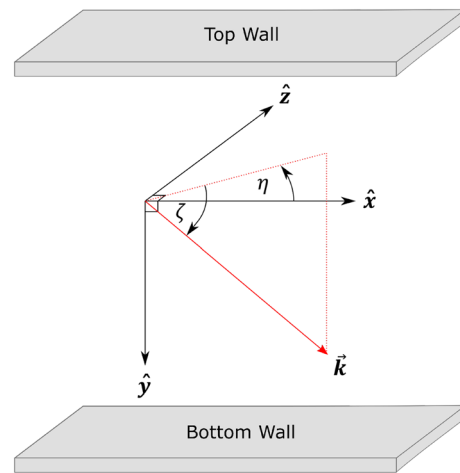

Fig. 16 Coordinate system for a generalized plane wave with wavevector $\vec{k}$

$$n_{ij}(\vec{x}, t) = A_{ij}\cos\left(\vec{k}_{ij} \cdot \vec{x} - 2\pi f_j t + \psi_{ij}\right), \tag{8}$$

where indices i and j represent the propagation direction and frequency, respectively, A_{ij} is the amplitude, $\vec{k}_{ij}$ is the wavevector, ψ_{ij} is a randomized phase, and $\vec{x} = (x, y, z)$. The phases ψ_{ij} are drawn randomly from the uniform distribution $[0, 2\pi)$. The wavevector is related to the disturbance frequency, f_j, by

$$k_{ij} = \frac{2\pi f_j}{U_i} \tag{9}$$

where $\vec{k}_{ij} \parallel \vec{U}_i$. The propagation velocity is U_∞ for entropic disturbances, and $U_\infty \cos \mu$ for acoustic disturbances. From the coordinate system in Fig. 16, the propagation angles are defined as

$$(\zeta, \eta) = \begin{cases} (\pm\mu, 0) & \text{for acoustic disturbances} \\ & \text{from top/bottom walls} \\ (0, \pm\mu) & \text{for acoustic disturbances} \\ & \text{from sidewalls} \\ (0, 0) & \text{for entropic disturbances.} \end{cases} \tag{10}$$

A pulse train of Gaussian envelopes is then created as

$$G_{1,ij}(\vec{x}, t) = \sum_{p=1}^{P_i+1} \exp\left[-\frac{\left[(\hat{k}_{ij} \cdot \vec{x} + s_{ip}) + \theta_{ij} - U_i t\right]^2}{2\sigma_{ij}^2}\right], \tag{11}$$

with

$$s_{ip} = \frac{U_i T}{P_i}(p - 1). \tag{12}$$

Here s_{ip} is the distance between wave packets along the propagation axis, P_i is the number of wave packets that propagate during the steady test time T, θ_{ij} is the randomized phase of the wave packet, and σ_{ij} is the width of the wave packet, which is linearly proportional to the wavelength of the disturbance. The pulse train propagates at the same velocity as the disturbance, i.e., the group and phase velocity are equal.

The Gaussian curve used to define the extent of the wave packet in the direction perpendicular to propagation is computed from

$$G_{2,ij}(\vec{x}, t) = \exp\left[-\frac{\left[\left(\hat{k}_{ij}^{\mathsf{T}} \cdot \vec{x} \right) \pm \vartheta_i \right]^2}{2\epsilon_{ij}^2} \right],\tag{13}$$

where $\hat{k}_{ij}^{\mathsf{T}}$ is within the xy-plane for entropic disturbances and acoustic disturbances from the top and bottom walls and in the xz-plane for acoustic disturbances from the sidewalls. ϵ_{ij} is the width of the Gaussian, which is specified to be linearly proportional to the wavelength of the disturbance, and ϑ_i is a translation relative to FLDI point 1 [$\vec{x} = (0, 0, 0)$ in the mode] used for disturbances propagating toward FLDI point 2 or 3.

Combining Eqs. (8), (11), and (13), the disturbance environment is given by

$$D(\vec{x}, t) = \frac{1}{\sqrt{N}} \sum_{i=1}^{M} \sum_{j=1}^{N} G_{2,ij} G_{1,ij} n_{ij},\tag{14}$$

where N and M are the number of frequency components and propagation directions, respectively. A scaling factor of $1/\sqrt{N}$ is used to keep the root-mean-square (RMS) constant as N increases for a fixed bandwidth (Lawson 2021). Since the wave packets have a finite width, only wave packets that pass through the FLDI points are modeled. The disturbance environment, $D(\vec{x}, t)$, is computed for the case of wave packets centered on FLDI point 1, 2, or 3. This gives $D_{\text{pt.1}}(\vec{x}, t)$, $D_{\text{pt.2}}(\vec{x}, t)$, and $D_{\text{pt.3}}(\vec{x}, t)$, respectively. The total fluctuation signal is then obtained from the summation of these three cases, that is,

$$D_{\text{tot}}(\vec{x}, t) = D_{\text{pt.1}}(\vec{x}, t) + D_{\text{pt.2}}(\vec{x}, t) + D_{\text{pt.3}}(\vec{x}, t) + W(t).\tag{15}$$

Finally, to match the electronic noise floor of the FLDI, Gaussian white noise, $W(t)$, was added.

The model was first tuned to match the experimental results for the case of no injection. The amplitudes A_{ij}, wave packet width σ_{ij}, and Gaussian width ϵ_{ij} were varied manually until the modeled signal provided a reasonable match to the ASD and CPSD results from the FLDI. All acoustic disturbances were treated identically. The model was computed with $N = 800$, a bandwidth of $f = [1 \times 10^4, 3 \times 10^6]$ Hz, and a sample rate of 6.77 MHz. Since the CPSD is dependent

on phase correlations, it was found that the modeled CPSD varied slightly for each computation as a result of the randomized phases. Therefore, the disturbance environment was iterated 60 times until the mean CPSDs reached convergence. For the ASD analysis, only one iteration was needed.

The PSD of the modeled fluctuations was calculated using Welch's method with Hanning windows of length 278 µs and 50% overlap, consistent with the parameters used in the experimental data analysis. The ASD was computed from the square root of the PSD. Presented in Fig. 17 is the ASD obtained at the location of FLDI points 1, 2, and 3 without any attenuation applied to the disturbances, as well as at FLDI point 2 with a 30% amplitude reduction for acoustic disturbances from the bottom wall. Compared to the experimental results in Fig. 12, the model matches the roll-off slope and high-frequency fluctuation amplitudes well. The model, however, has slightly higher fluctuation amplitudes around 300 kHz. It can also be seen that the ASD is essentially identical at each FLDI point, both with and without attenuation applied. This was noted in the experimental results and further indicates that a CPSD analysis is needed to assess the attenuation effects on the fluctuations.

The CPSD was calculated for modeled Mach-line and streamline signal pairs using Welch's method with Hanning windows of length 33 µs and 50% overlap, which again matches the parameters used in the experimental analysis. In Fig. 18, the Mach-line and streamline CPSDs for modeled fluctuations without any amplitude reductions are compared to the mean experimental CPSDs from the case of no injection. For the experimental Mach-line CPSD without
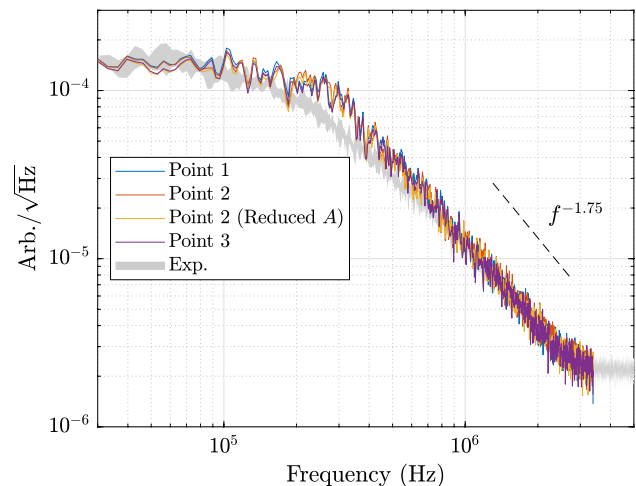

Fig. 17 Amplitude spectral density of modeled fluctuations at FLDI points 1, 2, and 3 without any attenuation and FLDI point 2 with a 30% amplitude reduction for acoustic disturbances from the bottom wall. The range of experimentally determined fluctuation amplitudes from various injection conditions (Fig. 12b) is shown in gray
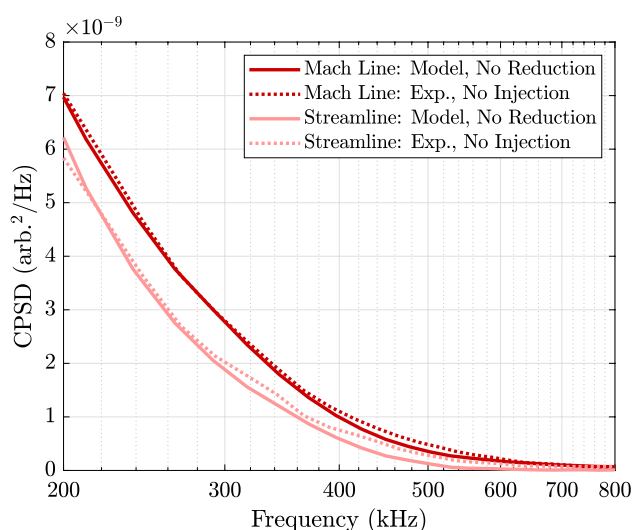
Fig. 18 Mean cross-power spectral densities of modeled fluctuations along a Mach line and streamline with no amplitude reductions compared to FLDI results with no injection

injection, the model with no amplitude reductions matches very well across all frequencies. The modeled CPSD along a streamline without amplitude reductions provides a reasonable match to the experimental results without injection, with a slight discrepancy around 400–600 kHz.

In Fig. 19, the CPSDs are presented for modeled fluctuations in cases for which the amplitudes of the acoustic disturbances from the bottom wall have been reduced by 0%, 15%, 30%, and 45%. The modeled CPSDs are compared to the mean experimental CPSDs along a Mach line and streamline from the case of no injection, and injection of 30% (Fig. 19a, b), 35% (Fig. 19c, d), and 40% (Fig. 19e, f) He/CO_2. Comparing the modeled Mach-line CPSD to the injection of 30% He/CO_2, it appears that an amplitude reduction of approximately 15–30% matches the experimental results, depending on the frequency. For the injection of 35% He/CO_2, the modeled Mach-line CPSD is consistent with a 30% amplitude reduction until approximately 400 kHz, and for the injection of 40% He/CO_2, an amplitude reduction of 15–30% provides good agreement. In Fig. 19b, d, and f, it can be seen that the modeled CPSD along a streamline is fairly insensitive to the amplitude reductions for acoustic disturbances from the bottom wall, with at most small differences between cases without amplitude reductions and with the maximum 45% reduction. These results are therefore also consistent with the 15–30% reduction that was found to match the Mach-line data for these experiments.

The mathematical disturbance model indicates that the presence of a vibrationally active gas species in the lower boundary layer resulted in a 15–30% reduction in measured acoustic-disturbance amplitudes. It should be noted that the injected mass flux of CO_2/He in the boundary layer is

relatively low (see "Appendix") and more significant attenuation could be expected if more injectant could be introduced without disturbing the boundary layer. The model also illustrates that reduced acoustic-disturbance amplitudes from the lower boundary have a minimal effect on the fluctuations correlated along a streamline, which is consistent with the experimental measurements. Thus, the disturbance model offers valuable insight into the sensitivity of these correlated measurements to entropic and acoustic-disturbance amplitudes.

6 Conclusion

The effects of vibrational nonequilibrium processes on acoustic noise radiated by a turbulent boundary layer were investigated in a Mach-2.8 shock tunnel. To first identify gas mixtures with strong absorption properties, measurements of attenuation coefficients were taken in a heated acoustic chamber. By varying the fraction of helium in He/CO_2 mixtures, the attenuation can be shifted to a desired frequency range; therefore, He/CO_2 mixtures are of particular interest for damping acoustic disturbances in high-speed wind tunnels. In the shock-tunnel facility, CO_2, N_2, He, and He/CO_2 mixtures were injected into the lower boundary layer of the flow through a porous plate located in the upstream region of the test section. A four-point FLDI was positioned above the turbulent boundary layer and was used to obtain simultaneous measurements of entropic disturbances propagating along streamlines and acoustic disturbances along Mach lines.

Amplitude spectral densities of the FLDI signals showed negligible differences between the cases with and without injection. Since the ASD at a single point is made up of disturbances propagating from all directions, however, a better indicator of the attenuation effects was the correlated fluctuations propagating from the bottom wall. Correlated fluctuations of FLDI signal pairs separated along a Mach line thus were analyzed using a cross-power spectral density for the various injection conditions. Baselines for comparison were provided both by similar correlations along a streamline (i.e., corresponding to entropic disturbances) and reference, no-injection experiments. Mixtures of 30%, 35%, and 40% He/CO_2 were found to have the most significant attenuation in Mach-line-correlated fluctuations. As minimal reductions in fluctuation power were measured along corresponding streamlines, it could be concluded that the vibrationally active gas species in the boundary layer primarily affected acoustic radiation and not entropic disturbances. Additional control cases with N_2 and He were also run to examine the influence of the injection itself and the density gradients within the boundary layer introduced by a light gas; minimal attenuation effects were seen in either case. Furthermore,

Fig. 19 Mean cross-power spectral densities of modeled fluctuations along a Mach line (**a**, **c**, **e**) and streamline (**b**, **d**, **f**) with 0%, 15%, 30%, and 45% reduced amplitudes for acoustic disturbances from the bottom wall. In each case, the disturbance model is compared to average FLDI results with no injection, and injection of 30%, 35%, and 40% He/CO_2 mixtures
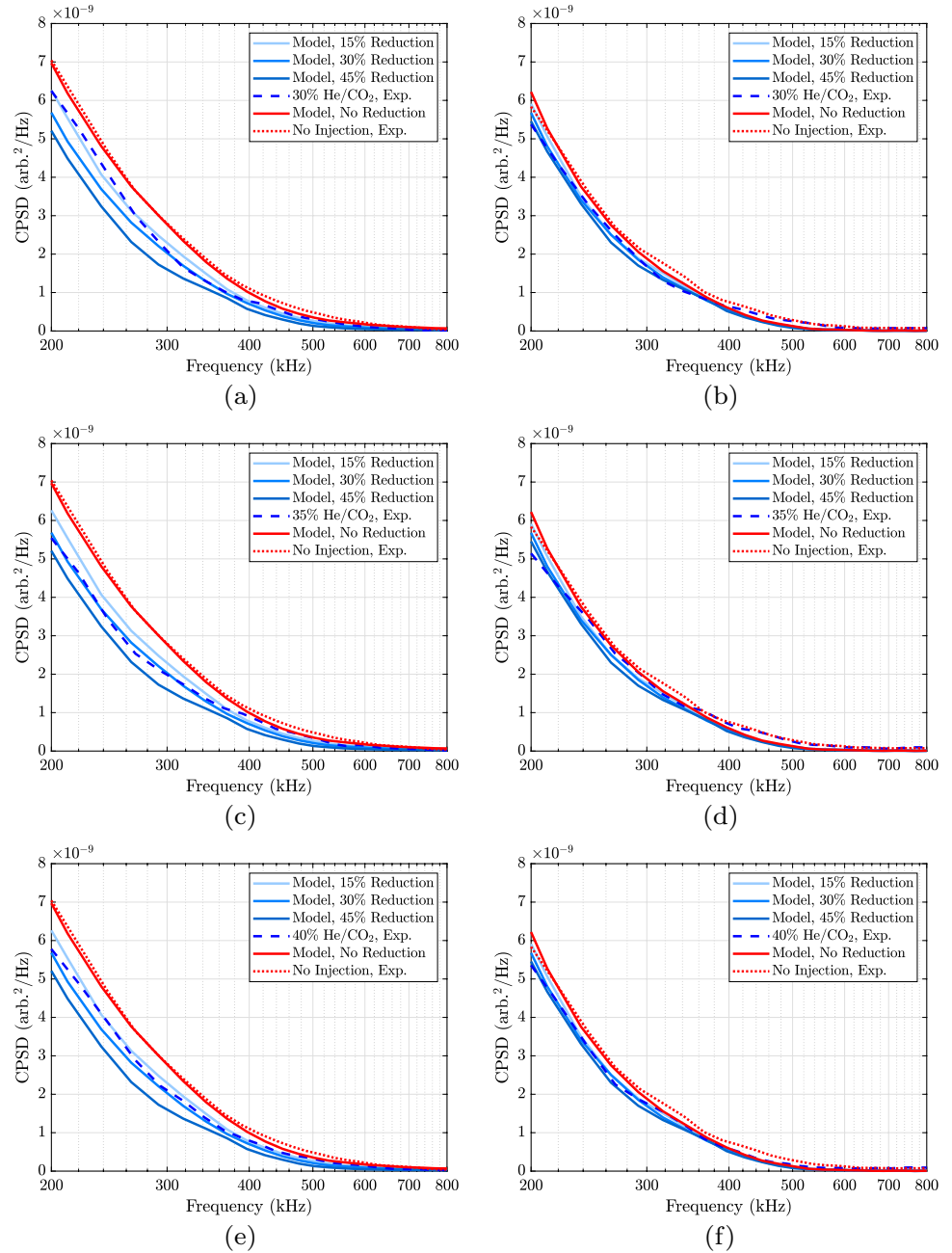
injection of pure CO_2 did not result in any significant attenuation, as expected: from the attenuation spectra measured in the acoustic chamber, it was determined that the addition of He to CO_2 results in a large increase in expected attenuation in the frequency range of $200 - 800$ kHz, which was consistent with the frequency range where significant attenuation was measured in the He/CO_2 mixtures (and where the FLDI instrument was most sensitive).

Since the correlated Mach-line fluctuations were not completely independent of other disturbances (i.e., acoustic noise propagating from the top and sidewall boundary layers and entropic disturbances) the measured decrease in CPSD was not necessarily a reliable quantitative indicator of the attenuation from the lower boundary layer. Therefore, a mathematical disturbance model was developed to isolate the effects of attenuation from this lower boundary layer alone. The disturbances were modeled as Gaussian wave packets propagating along Mach lines from the four test section walls and along streamlines. The model parameters were tuned to results from no-injection experiments, and the contribution from the lower boundary layer was then systematically reduced. An amplitude reduction of 15–30% was found to be consistent with the CPSD attenuation measured for He/CO_2 mixtures in experiments.

To the authors' knowledge, the results presented here provide the first reported measurements of nonequilibrium effects on turbulence-generated acoustic noise, and in particular, demonstration of the potential for damping of such noise. One limitation of this investigation however was the test facility, which was characterized by a brief test time and generally greater shot-to-shot variation than nonshock-driven facilities. This variation led to a relatively large degree of scatter in the attenuation results, making it difficult to draw firm conclusions from any single run. If a greater degree of attenuation was obtained by injecting the vibrationally active gas species into boundary layers along multiple walls, the effect of shot-to-shot variation could be diminished; however, this substantially increases the complexity of the injection system and may restrict optical access near the injection location. Additionally, if a porous plate with a larger surface area were to be used to inject a greater percentage of gas without disturbing the boundary layer, we might expect significantly enhanced attenuation effects. Additional work is also recommended to analyze the degree of dependence between the signals from the Mach-line and streamline pairs, for example, by varying the distance between the measurement pairs.

Appendix: Injection mass flow rate

As detailed by Moreira et al. (2004), the flow of a compressible fluid through a porous medium is described by the Forchheimer equation:

$$\frac{P_p^2 - P_\infty^2}{2P_p L} = \alpha_c \mu \frac{\dot{m}}{\rho_p A} + \beta_c \frac{\dot{m}^2}{\rho_p A^2},\tag{16}$$

where P_p is the plenum pressure underneath the porous plate, P_∞ is the pressure above the plate, L is the thickness of the plate, α_c is a friction-dependent permeability coefficient, β_c is an inertia-dependent permeability coefficient, μ is the dynamic viscosity, $\dot{m}$ is the mass flow rate, ρ_p is the density in the plenum, and A is the surface area of the plate. For the porous plate used in the present experiments, $\alpha_c = 111 \times 10^{10}$ m^{-2}, $\beta_c = 9 \times 10^5$ m^{-1}, $L = 5$ mm, and $A = 2.18 \times 10^{-3}$ m^2. Coefficients α_c and β_c were provided by the manufacturer, PORAL. Re-arranging Eq. (16), the mass flow rate can be expressed as

$$\dot{m} = -\frac{\alpha_c \mu A}{2\beta_c} + \left[\left(\frac{\alpha_c \mu A}{2\beta_c}\right)^2 + \frac{\rho_p A^2}{2\beta_c P_p L}\left(P_p^2 - P_\infty^2\right)\right]^{1/2}.\tag{17}$$

From Eq. (17), the total mass that flows through the plate can be determined from the integration of the mass flow rate throughout the injection process. The accuracy of Eq. (16)

for the present experiments can therefore be determined by comparing the total mass through the plate to the mass loss from the Ludwieg-tube reservoir, assuming there are no leaks around the plate. Using the ideal gas law, the change in mass inside the Ludwieg tube is given by

$$\Delta m_L = \frac{V}{RT}\left(P_{L,i} - P_{L,f}\right)\tag{18}$$

where V is the volume of the Ludwieg tube, T is the temperature, $P_{L,i}$ is the pressure in the tube prior to injection, and $P_{L,f}$ is the pressure in the tube upon reaching equilibrium after injection.

The ratio of the total mass through the plate, Δm_P, to the mass loss from the Ludwieg tube, Δm_L, was found for CO_2, N_2, and He for a range of injection pressures. In each case, the final pressure in the Ludwieg tube was recorded 10 s after injection. The change in mass ratio (i.e., the measured value divided by the Forchheimer prediction) is presented in Fig. 20 for various Ludwieg-tube reservoir pressures. It can be seen that the Forchheimer equation seems to overpredict the total mass through the porous plate for CO_2 and underpredict the total mass for He. For the injection test matrix in Table 2, the Ludwieg-tube reservoir pressures used to obtain the listed plenum pressures ranged from a low of $P_{L,i} = 4.95$ bar for He, up to $P_{L,i} = 6.40$ bar for various He/CO_2 mixtures. Therefore, from Fig. 20, we conclude that Forchheimer equation (16) is accurate to within approximately $\pm 18\%$ for the injection conditions of the present work.

The mass flow rate through the porous plate for the injection conditions in Table 2 can be compared to the mass flow rate of the lower boundary layer in the test section. From schlieren visualization, the boundary-layer
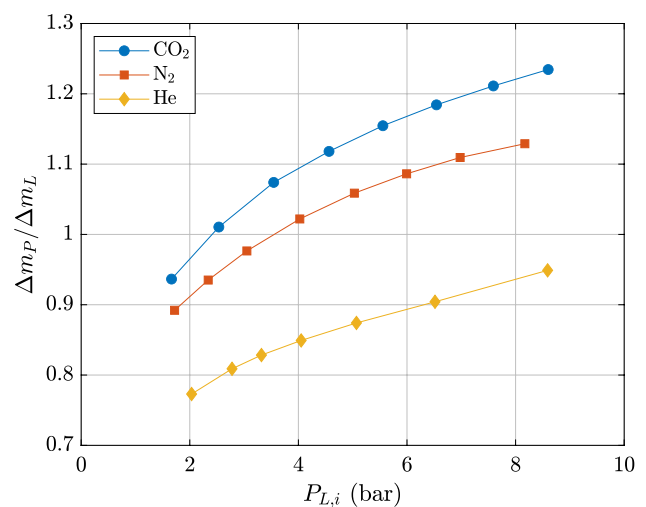
Fig. 20 The ratio of total mass through the porous plate, calculated with the Forchheimer equation, to mass loss in the Ludwieg tube for CO_2, N_2, and He at various Ludwieg-tube reservoir pressures

height at the location of the porous plate was determined to be approximately 5 mm without any injection occurring. To approximate the temperature and velocity profiles within the boundary layer, the coupled nonlinear partial differential equations for a compressible laminar boundary layer were solved as outlined by White and Majdalani (2006) [which follows the transformation approach of Illingworth (1950)]. The similarity solution was calculated with a cold wall temperature of 293 K (due to the short test time), a Prandtl number of 0.75, and a power-law approximation for the viscosity-temperature relation of a gas ($\mu \propto T^n$ with $n \approx 2/3$). This gives a peak temperature of 372 K in the boundary layer. The density profile is found with the ideal gas law, assuming a constant pressure across the boundary layer. The mass flow rate in the boundary layer is then computed with

$$\dot{m}_{BL} = W \int_0^\delta \rho(y)U(y)dy, \tag{19}$$

where $W = 50.8$ mm is the width of the flow region; this gives $\dot{m}_{BL} \approx 0.096$ kg/s.

The mass flow rate through the porous plate was determined with Eq. (17), where ρ_p is computed from the ideal gas law at plenum conditions. For a mixture, the coefficient of viscosity was calculated using

$$\mu = \sum_i \frac{X_i \mu_i}{X_i + \sum_{j \neq i}(X_i \phi_{ij})}, \tag{20}$$

with

$$\phi_{ij} = \frac{\left(1 + \left(\frac{\mu_i}{\mu_j}\right)^{\frac{1}{2}} \left(\frac{M_i}{M_j}\right)^{\frac{1}{4}}\right)^2}{\frac{4}{\sqrt{2}}\left(1 + \frac{M_i}{M_j}\right)^{\frac{1}{2}}}. \tag{21}$$

Here, X_i is the molar ratio of species i, M_i is the molar mass of species i, and ϕ_{ij} are Wilke's coefficients (Davidson 1993). The injection experiments were conducted at room temperature, and there was no temperature gradient across the porous plate under the assumption of a cold wall with a temperature of 293 K; therefore, the viscosity was taken at room temperature for each mixture component. Results of these calculations are presented in Table 3, where the ratio of the mean injection mass flow rates to the mass flow rate of the undisturbed lower boundary layer is provided in each condition. We see that the injected mass flux ranges from approximately 15–26% of the boundary-layer mass flux for He/CO$_2$, CO$_2$, and N$_2$ injection conditions and is considerably less for He injection (2.6%). Further downstream, near the FLDI measurement location, the boundary-layer height without injection is roughly twice the size of that at the location of the porous plate; therefore, the injected mass flux

Table 3 Relative mass flow rate through the porous plate for each injection condition

Injection gas	P_p (bar, $\pm$ 0.8%)	$\dot{m}/\dot{m}_{BL}$
50% He/CO$_2$	4.82	0.196
45% He/CO$_2$	3.98	0.155
40% He/CO$_2$	4.73	0.216
40% He/CO$_2$	3.99	0.166
40% He/CO$_2$	3.60	0.140
35% He/CO$_2$	4.14	0.187
35% He/CO$_2$	3.89	0.169
30% He/CO$_2$	3.87	0.178
30% He/CO$_2$	3.48	0.150
25% He/CO$_2$	4.14	0.209
25% He/CO$_2$	3.86	0.188
CO$_2$	4.18	0.263
CO$_2$	3.89	0.236
He	4.04	0.026
N$_2$	4.23	0.173
N$_2$	3.95	0.155

ratios downstream are roughly half of those presented in Table 3.

Declarations

References

Bass H (1973) Vibrational relaxation in CO$_2$/O$_2$ mixtures. J. Chem. Phys. 58(11):4783–4786

Bass H, Bauer HJ, Evans L (1972) Atmospheric absorption of sound: analytical expressions. J Acoust Soc Am 52(3B):821–825

Bauer H-J (1965) Phenomenological theory of the relaxation phenomena in gases. In: Mason WP (ed) Physical acoustics, vol 2, Part A. Academic Press, pp 47–131. https://doi.org/10.1016/B978-1-4832-2858-7.50010-7

Bauer HJ, Shields FD, Bass H (1972) Multimode vibrational relaxation in polyatomic molecules. J Chem Phys 57(11):4624–4628

Bhatia AB (1985) Ultrasonic absorption: an introduction to the theory of sound absorption and dispersion in gases, liquids, and solids. Courier Corporation, New York

Butler C (2021) Response of hypersonic boundary-layer disturbances to compression and expansion corners. PhD thesis, University of Maryland, College Park

Butler C, Laurence SJ (2019) HyperTERP: a newly commissioned hypersonic shock tunnel at the University of Maryland. In: AIAA Aviation 2019 Forum-2860

Butler CS, Laurence SJ (2021) Interaction of second-mode wave packets with an axisymmetric expansion corner. Exp Fluids 62(7):1–17

Ceruzzi A (2022) Development of two-point focused laser differential interferometry for applications in high-speed wind tunnels. PhD thesis, University of Maryland

Ceruzzi AP, Cadou CP (2022) Interpreting single-point and two-point focused laser differential interferometry in a turbulent jet. Exp Fluids 63(7):1–25

Chaudhry RS, Candler GV (2017) Computing measured spectra from hypersonic pitot probes with flow-parallel freestream disturbances. AIAA J 55:4155

Clarke JF, McChesney M, Talbot L (1964) The dynamics of real gases. Phys Today 17(11):76–78

Dain Y, Lueptow RM (2001) Acoustic attenuation in three-component gas mixtures-theory. J Acoust Soc Am 109(5):1955–1964

Davidson TA (1993) A simple and accurate method for calculating viscosity of gaseous mixtures. US Department of the Interior, Bureau of Mines

Demetriades A (1989) Growth of disturbances in a laminar boundary layer at Mach 3. Phys Fluids A Fluid Dyn 1(2):312–317

Duan L, Choudhari MM, Chou A, Munoz F, Radespiel R, Schilden T, Schröder W, Marineau EC, Casper KM, Chaudhry RS et al (2019) Characterization of freestream disturbances in conventional hypersonic wind tunnels. J Spacecr Rockets 56(2):357–368

Ejakov SG, Phillips S, Dain Y, Lueptow RM, Visser JH (2003) Acoustic attenuation in gas mixtures with nitrogen: experimental data and calculations. J Acoust Soc Am 113(4):1871–1879

Elliott OS, Greendyke R, Jewell JS, Komives JR (2019) Effect of CO_2 concentration in the hypersonic boundary layer on second mode disturbances. In: AIAA aviation 2019 Forum-2851

Fujii K, Hornung HG (2003) Experimental investigation of high-enthalpy effects on attachment-line boundary-layer transition. AIAA J 41(7):1282–1291

Fulghum MR (2014) Turbulence measurements in high-speed wind tunnels using focusing laser differential interferometry. PhD thesis, The Pennsylvania State University

Fuller TJ, Hsu AG, Sanchez-Gonzalez R, Dean JC, North SW, Bowersox RD (2014) Radiofrequency plasma stabilization of a low-Reynolds-number channel flow. J Fluid Mech 748:663–691

Gillespie G, Laurence SJ (2023) Measurement of acoustic attenuation in gas mixtures at elevated temperatures. In: AIAA Scitech 2023 Forum-0796

Gillespie GI, Ceruzzi AP, Laurence SJ (2022) A multi-point focused laser differential interferometer for characterizing freestream disturbances in hypersonic wind tunnels. Exp Fluids 63(11):1–17

Illingworth C (1950) Some solutions of the equations of flow of a viscous compressible fluid. In: Mathematical proceedings of the Cambridge philosophical society, vol 46. Cambridge University Press, pp 469–478

Jewell J, Wagnild R, Leyva I, Candler G, Shepherd J (2013) Transition within a hypervelocity boundary layer on a 5-degree half-angle cone in air/CO_2 mixtures. In: 51st AIAA aerospace sciences meeting including the new horizons forum and aerospace exposition-523

Kendall JM (1975) Wind tunnel experiments relating to supersonic and hypersonic boundary-layer transition. AIAA J 13(3):290–299

Kovasznay LS (1953) Turbulence in supersonic flow. J Aeronaut Sci 20(10):657–674

Lafferty J, Norris J (2007) Measurements of fluctuating pitot pressure, "tunnel noise," in the AEDC hypervelocity wind tunnel no. 9. In: 2007 US Air Force T &E Days-1678

Landau L, Teller E (1936) Zur theorie der schalldispersion. Phys Z Sowjetunion 10(1):34

Laufer J (1961) Aerodynamic noise in supersonic wind tunnels. J Aerosp Sci 28(9):685–692

Laufer J (1964) Some statistical properties of the pressure field radiated by a turbulent boundary layer. Phys Fluids 7(8):1191–1197

Laurence S, Wagner A, Hannemann K (2016) Experimental study of second-mode instability growth and breakdown in a hypersonic boundary layer using high-speed schlieren visualization. J Fluid Mech 797:471–503

Lawson JM (2021) Focused laser differential interferometry. PhD thesis, California Institute of Technology

Lewis J, Shields F (1967) Vibrational relaxation in carbon dioxide/helium mixtures. J Acoust Soc Am 41(1):100–102

Leyva I, Laurence S, Beierholm A, Hornung H, Wagnild R, Candler G (2009) Transition delay in hypervelocity boundary layers by means of CO_2/acoustic instability interactions. In: 47th AIAA aerospace sciences meeting including the new horizons forum and aerospace exposition-1287

Mahesh K, Lee S (1995) The interaction of an isotropic field of acoustic waves with a shock wave. J Fluid Mech 300:383–407

Moreira E, Innocentini M, Coury J (2004) Permeability of ceramic foams to compressible and incompressible flow. J Eur Ceram Soc 24(10–11):3209–3218

Morkovin MV (1957) On transition experiments at moderate supersonic speeds. J Aeronaut Sci 24(7):480–486

Morkovin MV (1959) On supersonic wind tunnels with low free-stream disturbances. J Appl Mech 26(3):319–324

Neville AG, Nompelis I, Subbareddy PK, Candler GV (2014) Effect of thermal non-equilibrium on compressible isotropic turbulence. In: 7th AIAA theoretical fluid mechanics conference-3204

Neville AG, Nompelis I, Subbareddy PK, Candler GV (2015) Thermal non-equilibrium effects in turbulent compressible shear flows. In: 45th AIAA fluid dynamics conference-3218

Parziale N, Shepherd J, Hornung H (2012) Reflected shock tunnel noise measurement by focused differential interferometry. In: 42nd AIAA fluid dynamics conference and exhibit-3261

Parziale N, Shepherd J, Hornung H (2014) Free-stream density perturbations in a reflected-shock tunnel. Exp Fluids 55:1–10

Parziale NJ (2013) Slender-body hypervelocity boundary-layer instability. PhD thesis, California Institute of Technology

Pate SR, Schueler C (1969) Radiated aerodynamic noise effects on boundary-layer transition in supersonic and hypersonic wind tunnels. AIAA J 7(3):450–457

Pee XY (2021) Unsteady shock propagation in a constant-area thermally choked flow: numerical and experimental investigations. PhD thesis, University of Maryland, College Park

Pee XY, Gillespie G, Laurence SJ (2021) Development of a direct-connect testing capability in the HyperTERP shock tunnel. In: AIAA Scitech 2021 forum-0650

Petculescu A, Hall B, Fraenzle R, Phillips S, Lueptow RM (2006) A prototype acoustic gas sensor based on attenuation. J Acoust Soc Am 120(4):1779–1782

Phillips OM (1960) On the generation of sound by supersonic turbulent shear layers. J Fluid Mech 9(1):1–28

Schmidt BE, Shepherd J (2015) Analysis of focused laser differential interferometry. Appl Opt 54(28):8459–8472

Schneider SP (2001) Effects of high-speed tunnel noise on laminar-turbulent transition. J Spacecr Rockets 38(3):323–333

Schneider SP (2008) Development of hypersonic quiet tunnels. J Spacecr Rockets 45(4):641–664

Schwartz R, Slawsky Z, Herzfeld K (1952) Calculation of vibrational relaxation times in gases. J Chem Phys 20(10):1591–1599

Settles GS, Fulghum MR (2016) The focusing laser differential interferometer, an instrument for localized turbulence measurements in refractive flows. J Fluids Eng 138(10):101402

Shields FD (1959) Measurements of thermal relaxation in CO_2 extended to 300C. J Acoust Soc Am 31(2):248–249

Shields FD (1970) On obtaining transition rates from sound absorption and dispersion curves. J Acoust Soc Am 47(5B):1262–1268

Siegman AE (1986) Lasers. University Science Books, Mill Valley

Smeets G (1972) Laser interferometer for high sensitivity measurements on transient phase objects. IEEE Trans Aerosp Electron Syst 8(2):186–190

Smeets G (1977) Flow diagnostics by laser interferometry. IEEE Trans Aerosp Electron Syst 13(2):82–90

Smeets G, George A (1971) Gas-dynamic investigations in a shock tube using a highly sensitive interferometer. Tech. rep, Institut Saint-Louis

Smeets G, George A (1973) Laser interferometer with phase compensation. NASA STI/Recon Technical Report N 77

Smeets G, George A (1975) Laser-differential interferometer applications in gas dynamics. Tech. rep, Institut Saint-Louis

Stetson K, Kimmel R (1992) On hypersonic boundary-layer stability. In: 30th Aerospace sciences meeting and exhibit-737

Wang JC, Springer GS (1973) Vibrational relaxation times in some hydrocarbons in the range 300–900 K. J Chem Phys 59(12):6556–6562

White FM, Majdalani J (2006) Viscous fluid flow, vol 3. McGraw-Hill, New York

Winter TG, Hill GL (1967) High-temperature ultrasonic measurements of rotational relaxation in hydrogen, deuterium, nitrogen, and oxygen. J Acoust Soc Am 42(4):848–858

Zhang C, Duan L, Choudhari MM (2018) Direct numerical simulation database for supersonic and hypersonic turbulent boundary layers. AIAA J 56(11):4297–4311

Zhang KS, Wang S, Zhu M, Ding Y, Hu Y (2013) Decoupling multimode vibrational relaxations in multi-component gas mixtures: analysis of sound relaxational absorption spectra. Chin Phys B 22(1):014305